Body size-dependent energy storage causes Kleiber's law scaling of the metabolic rate in planarians

Authors

Albert Thommen[1,2†], Steffen Werner[2,3†], Olga Frank[1†], Jenny Philipp[4], Oskar Knittelfelder[1], Yihui Quek[2,5], Karim Fahmy[4], Andrej Shevchenko[1], Benjamin M. Friedrich[2,6], Frank Jülicher[2*], Jochen C. Rink[1*].

Affiliations

[1] Max Planck Institute of Molecular Cell Biology and Genetics, Pfotenhauerstraße 108, 01307 Dresden, Germany.

[2] Max Planck Institute for the Physics of Complex Systems, Nöthnitzer Straße 38, 01187 Dresden, Germany.

[3] FOM Institute AMOLF, Science Park 104, 1098 XG, Amsterdam, The Netherlands.

[4] Helmholtz-Zentrum Dresden - Rossendorf, Institute of Resource Ecology, Bautzner Landstraße 400, 01328 Dresden, Germany.

[5] Massachusetts Institute of Technology, Cambridge, MA 02139, USA.

[6] Center for Advancing Electronics Dresden, Technische Universität Dresden, 01062 Dresden, Germany.

†These authors contributed equally to this work.

* Corresponding authors: julicher@pks.mpg.de, rink@mpi-cbg.de

Abstract

Kleiber's law, or the ¾-power law scaling of the metabolic rate with body mass, is considered one of the few quantitative laws in biology, yet its physiological basis remains unknown. Here, we report Kleiber's law scaling in the planarian *Schmidtea mediterranea*. Its reversible and life history-independent changes in adult body size over 2 orders of magnitude reveal that Kleiber's law does not emerge from the size-dependent decrease in cellular metabolic rate, but from a size-dependent increase in mass per cell. Through a combination of experiment and theoretical analysis of the organismal energy balance, we further show that the mass allometry is caused by body size dependent energy storage. Our results reveal the physiological origins of Kleiber's law in planarians and thus have general implications for understanding a fundamental scaling law in biology.

Introduction

Body size varies strikingly across animal phylogeny. From small crustaceans weighing a few ng to Blue Whales weighing in excess of 150 000 kg, body mass variations span more than 16 orders of magnitude (Makarieva et al., 2008; Sears & Calambokidis, 2002). In spite of such tremendous variation in scale and physiology, the organismal metabolic rate (*P;* defined as the heat produced by the organism per unit time measured in Watts, which is related to the rate of oxygen consumption (McDonald, 2002)) nevertheless follows a general scaling relationship with body mass (*M*). As originally described by Kleiber in 1932 (Max Kleiber, 1932), *P* can be expressed by a power-law of the form $P = aM^b$, with *b* being the scaling exponent and a proportionality constant *a*. Although reported values of *b* vary somewhat between studies or specific animal species, a value of $b \approx 3/4$ is typically observed (Banavar, Cooke, Rinaldo, & Maritan, 2014; Blaxter, 1989; Brody, 1945; Calder, 1984; Hemmingsen, 1960; M Kleiber, 1961; Peters, 1983; Schmidt-Nielsen, 1984; G B West & Brown, 2005; Whitfield, 2006) and this allometric relation between mass and metabolic rate is consequently referred to as the "three-quarter" or "Kleiber's law". This implies that the specific metabolic rate (*P*/*M*) decreases as body mass increases, which is commonly interpreted as reflecting a size-dependent decrease of cellular metabolic rates. Surprisingly, despite being known since more than 80 years and termed one of the few quantitative laws in biology (Geoffrey B West, 1999), the physiological basis of Kleiber's law remains under intense debate. The fact that all animals, irrespective of physiology, habitat or life style, obey Kleiber's law suggests a fundamental constraint in animal metabolism (G B West & Brown, 2005). Many hypotheses have been proposed that suggest a variety of origins of Kleiber's law. A major class of hypotheses are based on internal physical constraints (Glazier, 2005), for example space-filling fractal transportation networks (Goeffrey B West,

61 Brown, & Enquist, 1997) or size-dependent limitation of resource transport across external and
62 internal body surfaces (Davison, 1955; Mcmahon, 1973). Another class of hypotheses concerns
63 external ecological constraints, for example the optimization of body size for maximising
64 reproductive fitness (Kozlowski & Weiner, 1997). However, experimental validations have
65 proven difficult, due to inter-species differences in anatomy or ageing-associated physiological
66 changes within a species. As a result, all hypotheses regarding the origins of Kleiber's law
67 remain controversial also because a suitable model system has not been established.
68
69 Flatworm laboratory models offer interesting opportunities in this respect. Although usually
70 studied for their regenerative abilities and pluripotent adult stem cells (Reddien & Alvarado,
71 2004; Rink, 2012; Saló & Agata, 2012), the model species *S. mediterranea* and other planarians
72 display tremendous changes in body size. They grow when fed and literally shrink when starving
73 (Baguñà et al., 1990), which in *S. mediterranea* amounts to reversible body length fluctuations
74 between ~0.5 mm and ~20 mm. Such >40-fold changes in body length in a laboratory model
75 facilitate quantifications of P and M as pre-condition for applying and testing of theoretical
76 approaches. Moreover, the commonly studied asexual strain of *S. mediterranea* and other
77 asexual planarians do not seem to age, thus rendering their reversible size changes independent
78 of organismal aging (Glazier, 2005). Previous studies of metabolic rate scaling in planarians
79 suggest a size-dependence of O_2-consumption (Daly & Matthews, 1982; Hyman, 1919), but the
80 size dependence of P has so far not been systematically quantified. We here report that metabolic
81 rate scaling in *S. mediterranea* indeed follows Kleiber's law and we apply a combination of
82 experiments and theory to understand its physiological basis. Our analysis of the organismal
83 energy balance reveals that the size-dependent decrease in the specific metabolic rate does not

84 reflect a decrease in the metabolic rate per cell, but instead an increase in the mass per cell.
85 Further, we demonstrate that the cell mass allometry reflects a size-dependent increase in lipid
86 and glycogen stores. Our results therefore demonstrate that size-dependent energy storage causes
87 Kleiber's law scaling in planarians.
88
89
90 **Results**
91
92 **Planarians display Kleiber's law scaling of the metabolic rate**
93 Kleiber's law describes the scaling of metabolic rate with the mass of animals. In order to test
94 whether the tremendous body size fluctuations of *S. mediterranea* (*Figure 1A*) follow Kleiber's
95 law, we needed to devise methods to accurately quantify the mass and metabolic rate of
96 planarians.
97
98 To measure mass, we quantified both the dry and wet mass of individual planarians. Though dry
99 mass measurements avoid the challenging removal of residual water from the mucus-coated
100 animals, they are lethal and can therefore only be carried out once. As shown in *Figure 1B*, the
101 wet and dry mass of *S. mediterranea* vary over > 2 orders of magnitude. Moreover, the near-
102 constant ratio between wet and dry mass (~ 5; implying 80% water content) indicates minimal
103 variations of the water content and thus facile interconversion of the two mass measurements.
104 In order to quantify metabolic rate, we measured the heat generated by live planarians of
105 different sizes via microcalorimetry. Microcalorimetry measures the integrated heat generated by
106 metabolic processes inside the animal and therefore provides a pathway-independent measure of

107 total metabolic activity (Kemp & Guan, 1997). Cohorts of equally-sized 2 week-starved animals
108 were enclosed in vials and their heat emission measured over a period of > 24 h (*Figure 1 –*
109 *figure supplement 1*). Since animals were not immobilized, our measurements effectively reflect
110 the routine metabolic rate that is generally used for aquatic animals (Dall, 1986). As shown in
111 *Figure 1C*, the metabolic rate measurements increase with mass over nearly 3 orders of
112 magnitude (from ~ 0.02 to 10 μW). The data points can be fit with a single power law that
113 accurately describes the size-dependence of the metabolic rate across the entire size range.
114 Intriguingly, the value of the scale exponent is 0.75 ± 0.01 and thus identical with the ~ 0.75
115 exponent associated with Kleiber's law in inter-species comparisons. Consequently, the slope of
116 the planarian data points (red) exactly parallels the characteristic slope of extensive published
117 data sets of specific metabolic rate measurements (Makarieva et al., 2008) (*Figure 1D*). While
118 the offsets between endo- and ectotherm traces might reflect different temperature regimes as
119 previously noted (Hemmingsen, 1960; Makarieva et al., 2008), the common slopes stresses the
120 universal nature of the ¾ law exponent across animal phylogeny. The fact that the same power
121 law exponent is associated with the entire growth/degrowth-dependent body size interval of a
122 planarian suggests that the same underlying principles are at work and that *S. mediterranea* is
123 therefore a suitable model system for probing the physiological basis of Kleiber's law.
124

125 **Size-dependence of planarian growth/degrowth dynamics**

126 The physiological causes of planarian body size fluctuations are growth and degrowth.
127 Therefore, understanding their underlying regulation might provide insights into the size-
128 dependence of the metabolic rate. Planarian body size measurements are challenging due to their
129 soft and highly deformable bodies. We therefore adapted our semi-automated live-imaging

130 pipeline that extracts size measurements from multiple movie frames displaying the animals in
131 an extended body posture (Werner, Rink, Riedel-Kruse, & Friedrich, 2014). We found that plan
132 area provides the most robust size measure (*Figure 2 – figure supplement 1* and (Werner et al.,
133 2014)), which we therefore use in the following. One first important question is to what extent
134 size changes reflect a change in cell number. Since previous cell number estimates produced
135 conflicting results (Romero & Baguñà, 1991; Takeda, Nishimura, & Agata, 2009) we developed
136 two independent assays. First, we combined cell dissociation (Romero & Baguñà, 1991) with
137 automated counting of fluorescently stained nuclei (*Figure 2A, top* and *Figure 2 – figure*
138 *supplement 2*). Second, we used quantitative Western blotting to quantify the amount of the core
139 Histone H3 in whole worm lysates, which we found to increase linearly with the number of cells
140 (*Figure 2A, bottom*). Applying both assays to individually sized *S. mediterranea* revealed a close
141 agreement between the two methods and scaling of cell numbers with plan area by a power law
142 with the exponent 1.19 (*Figure 2B*), consistent with the previous conclusion that planarian body
143 size changes largely reflect changes in cell numbers (Baguñà et al., 1990). Further, knowledge of
144 the cell number/area scaling law allows the accurate interconversion of plan area into cell
145 numbers in the experiments below.
146
147 To measure growth and degrowth rates, we quantified the change in plan area of individual *S.*
148 *mediterranea* subjected to feeding at regular time intervals (*Figure 2C*) or continuous starvation
149 (*Figure 2D*). Although individual measurements were noisy due to the aforementioned size
150 quantification challenges, the data on >100 animals cumulatively reveal stereotypic time
151 trajectories for both growth and degrowth (*Figure 2C-D, insets*). Therefore, planarian growth
152 and degrowth dynamics are highly coordinated at the organismal level and our data are suitable

153 for extracting the underlying rate constants. As shown in *Figure 2E*, we found that the growth
154 rate of *S. mediterranea* decreases with body size, consistent with previous data (Baguñà et al.,
155 1990). Unexpectedly, our analysis additionally revealed a similar size dependence of the
156 degrowth rate. Interestingly, both growth and degrowth rates appeared to be largely independent
157 of feeding history and thus solely a function of size (*Figure 2 – figure supplement 3A*). Taken
158 together, our findings demonstrate that not only the specific metabolic rate (*Figure 1C-D*), but
159 also the growth/degrowth rates decrease with body size in *S. mediterranea*.
160

161 **Systems-level control of planarian growth dynamics**

162 Since growth reflects the metabolic assimilation of environmental resources and degrowth their
163 subsequent catabolism, both are related to the overall metabolic rate of the animal. Therefore, the
164 size dependence of growth/degrowth (*Figure 2E*) and metabolic rate (*Figure 1C-D*) might reflect
165 a common physiological origin of the underlying scaling laws. We therefore devised a theoretical
166 framework of planarian growth/degrowth as a function of the metabolic energy budget (*Figure*
167 *3A*). The central element of our model and previous approaches (Hou et al., 2008; Kooijman,
168 2009) is the organismal energy content E, which represents the sum of all physiologically
169 accessible energy stores (e.g., carbohydrates, lipids and proteins). The energy content E fuels all
170 metabolic processes within the animal, which collectively convert E into heat as measured by our
171 microcalorimetry approach (*Figure 1C-D*). Hence, starvation results in a decrease of E, overall
172 net catabolism and degrowth. However, E increases if the influx of energy obtained from the
173 food (J) exceeds the energy lost through heat (P), which leads to net assimilation of resources
174 and thus growth. The fact that planarians grow/degrow largely by a change in total cell numbers
175 (*Figure 2B*) (Baguñà et al., 1990; Romero & Baguñà, 1991), fundamentally interconnects the

organismal energy balance to organismal cell numbers. While excess energy from food intake stimulates increased cell proliferation (Baguñà, 1974) and growth, a starvation-induced net loss of energy decreases total cell numbers and thus, body size. Therefore, our framework relates changes in cell number during growth/degrowth to the energy content of the animal (*Figure 3A*). Importantly, our model does not make any assumptions regarding the underlying cellular or metabolic mechanisms, but simply states the physical energy balance of planarians.

With our quantitative data as experimental constraint (*Figure 2C-E*), the model allows us to explore hypothetical systems-level control paradigms of growth/degrowth dynamics (see also *Figure 3 – figure supplement 1*). In the first paradigm (*Figure 3B, left column*), dynamic changes in the organismal energy content depend on feeding conditions. Changes in cell number (e.g., rates of cell division and/or cell death) depend on the energy content per cell (*Figure 3 – figure supplement 2*). Consequently, two planarians with the same cell number might have different energy levels depending on the respective feeding history. In paradigm 2 (*Figure 3B, centre column*), the energy content is proportional to total cell number, i.e. it scales isometrically. Thus, growth occurs when "surplus" energy obtained from food is converted into new cells, whereas degrowth is the consequence of catabolism of existing cells in order to replenish metabolic energy. In paradigm 3, the energy content is also tightly coupled to cell number, but scales in a size-dependent manner with a characteristic exponent c, i.e. it scales allometrically. Theoretical analysis reveals that all three paradigms can approximate the measured growth/degrowth dynamics (*Figure 3C*). However, they differ in their specific predictions of the scaling behaviours of E, P and J with organismal cell number N (*Figure 3B*).

199 In order to experimentally distinguish between the paradigms, we consequently quantified *E*, *P*
200 and *J* as a function of cell number (*N*). In order to obtain values for *P*/*N* (metabolic rate/cell), we
201 converted our measurements of *P* as a function of dry mass (*Figure 1 – figure supplement 1B*)
202 using the scaling laws for *N* and dry mass with plan area (*Figure 2B* and *Figure 3 – figure*
203 *supplement 3A*). As shown in *Figure 3D*, the *P*/*N* estimates are of the order of 1 pW, similar to
204 the average metabolic rate of a human cell (Bianconi et al., 2013; Purves & Sadava, 2004).
205 Further, *P*/*N* is essentially independent of organismal cell number and animal size (scale
206 exponent 0.05 +/- 0.02), which rules out paradigm 2 (*Figure 3B*) as possible control principle.
207 The size *independence* of *P*/*N* is further intriguing, as it implies that the size *dependence* of *P/M*
208 as foundational basis of Kleiber's law originates from size dependencies of *M/N* (mass per cell;
209 see below).
210
211 To measure the food intake *J*, we developed an assay based on the homogenous dispersion of a
212 known amount of small fluorescent beads in a known volume of planarian sustenance food (liver
213 paste). Lysis of pre-sized animals immediately after feeding and quantification of bead numbers
214 in the lysate thus provided a measure of the ingested food volume as a function of size (*Figure 3*
215 *– figure supplement 3B-D*). Although individual measurements varied significantly (likely
216 reflecting inter-animal differences under our *ad libitum* feeding conditions), *J*/*N* did not display a
217 clear size dependence (exponent 0.00 ± 0.03) (*Figure 3E*). Therefore, the volume of ingested
218 food and thus energy uptake remains proportional to organismal cell number across the entire
219 size range, which argues against both paradigms 1 and 2 (*Figure 3B*).
220

221 To approximate the energy content E of entire worms, we turned to bomb calorimetry. This
222 method quantifies the heat release upon complete combustion of dried tissue in pure oxygen,
223 thus providing a measure of gross energy content (McDonald, 2002). Our assay conditions
224 allowed reproducible quantification of E of as little as 3 mg of dried tissue (*Figure 3 – figure*
225 *supplement 3E*), corresponding to 200 planarians of a length of 2 mm (*Figure 3 – figure*
226 *supplement 3A* and *Figure 2 – figure supplement 1D*). Intriguingly, E/N significantly increased
227 with organismal cell numbers (scaling exponent 0.38 ± 0.03, *Figure 3F*), as assumed by
228 paradigm 3 (*Figure 3B*). Moreover, the experimentally measured scaling exponent of the energy
229 content agrees quantitatively with the prediction of paradigm 3 on basis of the experimentally
230 measured growth/degrowth rates (*Figure 3F*; black solid line). The experimentally measured
231 gross energy content and the physiologically accessible energy content E (green and black solid
232 lines in *Figure 3F*) differ by a constant factor (2). The fact that the scaling exponent follows the
233 prediction of paradigm 3 demonstrates the quantitative agreement between model and
234 experiment and identifies size-dependent energy storage as systems-level control paradigm of
235 planarian growth/degrowth dynamics.
236
237 **Size dependence of physiological energy stores**
238 Since animals store energy in the form of biochemical compounds, size-dependent energy
239 storage should consequently result in biochemically measurable effects. Little is currently known
240 about planarian energy metabolism, but animals generally store metabolic energy in the form of
241 triglycerides (TGs) inside lipid droplets (Birsoy, Festuccia, & Laplante, 2013). We therefore
242 stained cross-sections of large and small animals with the lipid droplet marker LD540 (Spandl,
243 White, Peychl, & Thiele, 2009). Both revealed prominent lipid droplets primarily within the

244 intestinal epithelium, thus suggesting that the planarian intestine serves as a fat storage organ, as
245 in *C. elegans* (Mak, 2012). However, the amount and size of the droplets per cell notably
246 increased in large animals (*Figure 4A*). To obtain a quantitative measure of the lipid content size-
247 dependence, we optimized total lipid extraction for planarians (*Figure 4 – figure supplement 1A*)
248 and used mass spectrometry to measure the absolute amounts of various lipid classes (*Figure 4 –*
249 *figure supplement 1B*). The 88-fold increase in TGs per unit cell in large planarians as compared
250 to small animals (*Figure 4B*) demonstrates a striking size dependence of lipid stores in *S.*
251 *mediterranea*.
252
253 To further assess a possible size dependence of carbohydrate stores, we applied Best's Carmine
254 stain to cross-sections of large and small animals in order to probe for glycogen granules (*Figure*
255 *4C, left*). Comparison between adjacent sections with and without amyloglucosidase pre-
256 treatment as specificity control (*Figure 4C, right*) together with the expression patterns of
257 glycogen synthesis genes (*Figure 4 – figure supplement 1C*) both indicate a storage role of the
258 planarian intestine for glycogen granules, thus again emphasizing the organ's likely central role
259 in energy homeostasis. Interestingly, also the intensity of glycogen staining appeared stronger in
260 large animals (*Figure 4C, right*) and the quantification of glycogen content in animal extracts by
261 an enzyme-based assay (*Figure 4 – figure supplement 1D-F*) demonstrated a > 8-fold increase in
262 the amount of glycogen/cell in large over small animals (*Figure 4*). Therefore, both the lipid and
263 carbohydrates stores are strongly size-dependent in *S. mediterranea*, which conclusively
264 confirms our model's prediction of size-dependent energy storage as a systems-level control
265 paradigm of planarian growth and degrowth.
266

267 **Energy reserves and cell number govern Kleiber's law in planarians**

268 The size-dependent increase in the mass of lipid and glycogen stores is intriguing also in light of
269 the previous indications that Kleiber's law in planarians might originate from a size-dependent
270 increase in mass per cell, rather than a decrease in metabolic rate (*Figure 3D*). To explore this
271 potential link between the regulation of growth dynamics and Kleiber's law, we first investigated
272 the relative contributions of mass allometries to the emergence of the ¾ exponent. As a direct
273 test, we derived the size dependence of cell numbers versus mass, using the various scaling laws
274 established during the course of this study. As shown in *Figure 5A*, cell numbers scale with wet
275 and dry mass with scale exponents of 0.74 ± 0.01 and 0.72 ± 0.01, respectively. This
276 demonstrates that the mass per cell indeed increases disproportionately with size and with a very
277 similar scaling exponent as for Kleiber's law (*Figure 1C*). In conjunction with the practically
278 size-independent scaling of cell number and metabolic rate (Figure 5B, scaling exponent 0.96 ±
279 0.02), these data demonstrate conclusively that the ¾ exponent of the metabolic rate/mass scaling
280 law derives from the underlying scaling law of mass/cell.

281

282 To quantitatively assess the contributions of energy stores to the mass/cell scaling exponent and
283 thus to Kleiber's law, we analysed the composition of the dry mass in small, medium and large
284 animals. In addition to storage lipids and glycogen, we quantified total protein (*Figure 5 – figure*
285 *supplement 1A*), non-glycogen carbohydrates (*Figure 5 – figure supplement 1B-C*) and other
286 polar and non-polar lipids (*Figure 4 – figure supplement 1B*). In comparison with the 8 and 88-
287 fold increase of glycogen and TG contributions to dry mass/cell, the relative contribution of
288 protein, other polar/non-polar lipids and non-glycogen carbohydrates varied less between small
289 and large animals (*Figure 5C*). Our quantitative assays further allowed us to assess the absolute

290 mass contribution of each compound class to the size-dependent dry mass increase and thus to
291 the origins of the ¾ exponent. Intriguingly, the latter was largely explained by the mass of
292 triglycerides and glycogen, with additional minor contributions from other carbohydrates,
293 polar/non-polar lipids and protein (*Figure 5C*). Overall, our results therefore demonstrate that
294 size-dependent energy storage causes Kleiber's law scaling in *S. mediterranea.*
295
296
297 **Discussion**
298 Here, we make use of the dramatic and reversible body size changes in the planarian *S.*
299 *mediterranea* to probe the physiological basis of Kleiber's law. Contrary to comparative
300 approaches that generally start from *a priori* assumptions and subsequently examine large multi-
301 species data sets for supporting evidence, our finding that planarians obey Kleiber's law scaling
302 allows us to bring an experimental approach in a model system to bear on the problem.
303 Growth/degrowth in asexual planarians (e.g., the strain examined here) reversibly scales the size
304 of a fully developed adult body plan. This likely exposes size-dependent physiological
305 constraints more clearly than in other animals, where ontogenic growth is often accompanied by
306 developmental changes. Our combination of quantitative and theoretical analysis of growth and
307 degrowth dynamics demonstrate that Kleiber's law scaling in planarians originates not from a
308 size-dependent decrease in specific metabolic rate, but from a size-dependent increase in average
309 cellular mass. Further, our demonstration that the ¾ exponent is largely caused by size-
310 dependent lipid and glycogen stores firmly ties the physiological origins of planarian Kleiber's
311 law scaling to energy metabolism. To our knowledge, our results provide a first experimentally
312 founded demonstration of the physiological origins of Kleiber's law scaling in an animal species.

The fact that we find the cellular metabolic rate to be size-independent contrasts with multiple proposals that envisage the origins of Kleiber's law in a size-dependent decrease of cellular metabolic activity, e.g., by decreasing mitochondrial density (Smith, 1956). However, our use of microcalorimetry as a pathway-independent read-out of the post-absorptive metabolic rate leaves open the possibility of size-dependencies in the use of specific metabolic pathways. In this context, it is interesting to note that the ratio between our experimentally measured gross energy content (by bomb calorimetry) and net energy usage (modelling of growth dynamics data on basis of paradigm 3; *Figure 3B*) remains constant across the entire size range (*Figure 3F*). This entails that the metabolic processes that assimilate ingested food or catabolise energy stores are largely size-independent (constant food conversion rate of 2.6, in line with other aquatic organisms (Tacon & Metian, 2008); *Figure 3 – figure supplement 3F*). Instead, what changes in a size-dependent manner is the relative proportion of organismal energy resources that is channelled into the formation of metabolically active cells versus metabolically inert energy stores. While small planarians "invest" largely in new cells and little into stores, large animals predominantly store ingested food energy and produce few new cells. Allometric scaling of fat content with mass in mammals (Scale exponent 1.19 (Calder, 1984; Pitts & Bullard, 1968)) raises the possibility that similar physiological trade-offs may contribute to P/M allometries in other animals.

Our demonstration of size-dependent energy storage as physiological cause of Kleiber's law in planarians also narrows the quest for a quantitative understanding of the ¾ scale exponent. Interestingly, the trade-off between energy storage and addition of new cells converges on a

central premise of the Dynamic Energy Budget (DEB) theory, which can derive the ¾ exponent out of the assumption of surface-limited energy store mobilization (Maino, Kearney, Nisbet, & Kooijman, 2014). However, planarians assimilate and distribute metabolic energy via the branched tubular network of their intestine (Forsthoefel, Park, & Newmark, 2011) (termed "gastrovasculature"). This also makes the intrinsic transport capacity limitations of space-filling fractal networks a possible origin of the ¾ exponent, as per the WEB theory (Goeffrey B West et al., 1997). Further, it is also conceivable that neither process is rate-limiting and that size-dependent energy storage emerges as a consequence of a size-dependence of stem cell division probabilities, for example. Importantly, our results establish an experimental system for the systematic experimental evaluation of these and other theories and thus also the mechanistic basis of Kleiber's law.

References

Baguñà, J. (1974). Dramatic mitotic response in planarians after feeding, and a hypothesis for the control mechanism. *Journal of Experimental Zoology*, *190*(1), 117–122. http://doi.org/10.1002/jez.1401900111

Baguñà, J., Romero, R., Saló, E., Collet, J., Carme, A., Ribas, M., … Bueno, D. (1990). Growth, degrowth and regeneration as developmental phenoma in adult freshwater planarians. In H.-J. Marthy (Ed.), *Experimental Embryology in Aquatic Plants and Animals* (Plenum Pre, pp. 129–162). New York.

Banavar, J. R., Cooke, T. J., Rinaldo, A., & Maritan, A. (2014). Form, function, and evolution of living organisms. *Proceedings of the National Academy of Sciences*, *111*(9), 3332–3337.

http://doi.org/10.1073/pnas.1401336111

Berthold, M. R., Cebron, N., Dill, F., Gabriel, T. R., Kötter, T., Meinl, T., … Wiswedel, B. (2007). The Konstanz Information Miner. In W. Gaul, M. Vichi, & C. Weihs (Eds.), *Studies in Classification, Data Analysis, and Knowledge Organization* (pp. 319–326). Springer.

Bianconi, E., Piovesan, A., Facchin, F., Beraudi, A., Casadei, R., Frabetti, F., … Canaider, S. (2013). An estimation of the number of cells in the human body. *Annals of Human Biology*, *40*(6), 463–471. http://doi.org/10.3109/03014460.2013.807878

Birsoy, K., Festuccia, W. T., & Laplante, M. (2013). A comparative perspective on lipid storage in animals. *Journal of Cell Science*, *126*(7), 1541–1552. http://doi.org/10.1242/jcs.104992

Blaxter, K. (1989). *Energy Metabolism in Animals and Man*. Cambridge University Press. Retrieved from https://books.google.de/books?id=mAw5AAAAIAAJ

Bligh, E. G., & Dyer, W. J. (1959). A rapid method of total lipid extraction and purification. *Canadian Journal of Biochemistry and Physiology*, *37*(8), 911–917. http://doi.org/dx.doi.org/10,1139/cjm2014-0700

Brody, S. (1945). *Bioenergetics and Growth: With Special Reference to the Efficiency Complex in Domestic Animals*. New York: Van Nostrand Reinhold.

Calder, W. A. (1984). *Size, Function, and Life History*. Cambridge, MA: Harvard University Press.

Carpenter, A. E., Jones, T. R., Lamprecht, M. R., Clarke, C., Kang, I. H., Friman, O., … Sabatini, D. M. (2006). CellProfiler: image analysis software for identifying and quantifying cell phenotypes. *Genome Biology*, *7*(10), R100. http://doi.org/10.1186/gb-2006-

7-10-r100

Dall, W. (1986). Estimation of routine metabolic-rate in a penaeid prawn, Penaeus-Esculentus Haswell. *Journal of Experimental Marine Biology and Ecology*, *96*(1), 57–74. http://doi.org/10.1016/0022-0981(86)90013-4

Daly, J. J., & Matthews, H. M. (1982). Effect of weight and temperature upon oxygen consumption of the land planarian bipalium kewense. *Physiological Zoology*, *55*(2), 148–154.

Davison, J. (1955). Body weight, cell surface, and metabolic rate in anuran amphibia. *The Biological Bulletin*, *109*(3), 407–419. http://doi.org/10.2307/1539173

Forsthoefel, D. J., Park, A. E., & Newmark, P. A. (2011). Stem cell-based growth, regeneration, and remodeling of the planarian intestine. *Developmental Biology*, *356*(2), 445–459. http://doi.org/10.1016/j.ydbio.2011.05.669

Glazier, D. S. (2005). Beyond the variation in the intra- and interspecific scaling of metabolic rate in animals. *Biological Reviews*, *80*, 611–662. http://doi.org/10.1017/S1464793105006834

Hemmingsen, A. M. (1960). *Energy metabolism as related to body size and respiratory surfaces and its evolution*. *Reports of the Steno Memorial Hospital and then Nordisk Insulinlaboratorium Gentofte, Denmark*. Copenhagen: Nordisk Insulinlaboratorium; Gentofte and Strodam Biological Laboratory; Hillerod.

Herzog, R., Schuhmann, K., Schwudke, D., Sampaio, J. L., Bornstein, S. R., Schroeder, M., & Shevchenko, A. (2012). LipidXplorer: a software for consensual cross-platform lipidomics.

PloS One, *7*(1), e29851. http://doi.org/10.1371/journal.pone.0029851

Hou, C., Zuo, W., Moses, M. E., Woodruff, W. H., Brown, J. H., & West, G. B. (2008). Energy uptake and allocation during ontogeny. *Science*, *322*(5902), 736–739. http://doi.org/10.1126/science.1162302

Hyman, L. H. (1919). Physiological studies on planaria. III oxygen consumption in relation to age (size) differences. *Biological Bulletin*, *37*(6), 388–403. Retrieved from http://www.jstor.org/stable/1536374

Ke, M.-T., Fujimoto, S., & Imai, T. (2013). SeeDB : a simple and morphology-preserving optical clearing agent for neuronal circuit reconstruction. *Nature Neuroscience*, *16*(8), 1154–1161. http://doi.org/10.1038/nn.3447

Kemp, R. B., & Guan, Y. (1997). Heat flux and the calorimetric-respirometric ratio as measures of catabolic flux in mammalian cells. *Thermochimica Acta*, *300*(1–2), 199–211. http://doi.org/10.1016/S0040-6031(96)03125-5

King, R. S., & Newmark, P. A. (2013). In situ hybridization protocol for enhanced detection of gene expression in the planarian Schmidtea mediterranea. *BMC Developmental Biology*, *13*(1), 8. http://doi.org/10.1186/1471-213X-13-8

Kleiber, M. (1932). Body size and metabolism. *Hilgardia: A Journal of Agricultural Science*, *6*(11), 315–353. http://doi.org/10.1017/CBO9781107415324.004

Kleiber, M. (1961). *The Fire of Life: an Introduction to Animal Energetics*. New York: Wiley. Retrieved from https://books.google.de/books?id=pctqAAAAMAAJ

Kooijman, S. A. L. M. (2009). *Dynamic Energy Budget theory for metabolic organisation*.

Cambridge: Cambridge University Press. Retrieved from http://ebooks.cambridge.org/ref/id/CBO9780511805400

Kozlowski, J., & Weiner, J. (1997). Interspecific allometries are by-products of body size optimization. *The American Naturalist*, *149*(2), 352–380. http://doi.org/https://doi.org/10.1086/285994

Maino, J. L., Kearney, M. R., Nisbet, R. M., & Kooijman, S. A. L. M. (2014). Reconciling theories for metabolic scaling. *Journal of Animal Ecology*, *83*(1), 20–29. http://doi.org/10.1111/1365-2656.12085

Mak, H. Y. (2012). Lipid droplets as fat storage organelles in *Caenorhabditis elegans*. *Journal of Lipid Research*, *53*(1), 28–33. http://doi.org/10.1194/jlr.R021006

Makarieva, A. M., Gorshkov, V. G., Li, B.-L., Chown, S. L., Reich, P. B., & Gavrilov, V. M. (2008). Mean mass-specific metabolic rates are strikingly similar across life's major domains: Evidence for life's metabolic optimum. *Proceedings of the National Academy of Sciences of the United States of America*, *105*(44), 16994–9. Copyright (2008) National Academy of Sciences. http://doi.org/10.1073/pnas.0802148105

McDonald, P. (2002). *Animal Nutrition*. Pearson Education. Retrieved from https://books.google.de/books?id=jxUXns9laAEC

Mcmahon, T. (1973). Size and shape in biology. *Science*, *179*(4079), 1201-12–4. http://doi.org/10.1126/science.179.4079.1201

Mulisch, M., & Welsch, U. (Eds.). (2010). *Romeis - Mikroskopische Technik* (18th ed.). Berlin Heidelberg: Spektrum Akademischer Verlag (Springer).

443 Nutrient report of calf liver. (2016). Retrieved February 7, 2018, from
444 https://ndb.nal.usda.gov/ndb/foods/show/5301?n1=%7BQv%3D1%7D&fgcd=&man=&lfac
445 et=&count=&max=50&sort=default&qlookup=calf+liver&offset=&format=Full&new=&m
446 easureby=&Qv=1&ds=&qt=&qp=&qa=&qn=&q=&ing=

447 Overmoyer, B. A., McLaren, C. E., & Brittenham, G. M. (1987). Uniformity of liver density and
448 nonheme (storage) iron distribution. *Arch Pathol Lab Med*, *111*(6), 549–54.

449 Pearson, B. J., Eisenhoffer, G. T., Gurley, K. A., Rink, J. C., Miller, D. E., & Alvarado, A. S.
450 (2009). Formaldehyde-based whole-mount in situ hybridization method for planarians.
451 *Developmental Dynamics*, *238*(2), 443–450. http://doi.org/10.1002/dvdy.21849

452 Peters, R. H. (1983). *The Ecological Implications of Body Size*. Cambridge: Cambridge
453 University Press. http://doi.org/doi:10.1017/CBO9780511608551

454 Pitts, G. C., & Bullard, T. R. (1968). Some interspecific aspects of body composition in
455 mammals. In *Body Composition in Animals and Man* (pp. 45–70). Washington, D.C.:
456 National Academy of Science, Pub No 1598.

457 Purves, W. K., & Sadava, D. (2004). *Life: The Science of Biology* (7th ed.). New York: Freeman.

458 Rasouli, M., Shokri-Afra, H., & Ostovar-Ravari, A. (2015). A new protocol for separation of
459 acid soluble and insoluble fractions from total glycogen and simultaneous measurements.
460 *European Review for Medical and Pharmacological Sciences*, *19*(10), 1785–1789.

461 Reddien, P. W., & Alvarado, A. S. (2004). Fundamentals of planarian regeneration. *Annu. Rev.*
462 *Cell Dev. Biol*, *20*, 725–57. http://doi.org/10.1146/annurev.cellbio.20.010403.095114

463 Rink, J. C. (2012). Stem cell systems and regeneration in planaria. *Development Genes and*

Evolution. http://doi.org/10.1007/s00427-012-0426-4

Romero, R., & Baguñà, J. (1991). Quantitative cellular analysis of growth and reproduction in freshwater planarians (Turbellaria; Tricladida). I. A cellular description of the intact organism. *Invertebrate Reproduction & Development*, *19*(2), 157–165. http://doi.org/10.1080/07924259.1991.9672170

Sales, S., Graessler, J., Ciucci, S., Al-Atrib, R., Vihervaara, T., Schuhmann, K., … Shevchenko, A. (2016). Gender, contraceptives and individual metabolic predisposition shape a healthy plasma lipidome. *Scientific Reports*, *6*(May), 27710. http://doi.org/10.1038/srep27710

Sales, S., Knittelfelder, O., & Shevchenko, A. (2017). Lipidomics of Human Blood Plasma by High-Resolution Shotgun Mass Spectrometry. In *Methods in Molecular Biology* (Vol. 1619, pp. 203–212). http://doi.org/10.1007/978-1-4939-7057-5_16

Saló, E., & Agata, K. (2012). The planaria model system. *The International Journal of Developmental Biology*, *56*, 1–4. http://doi.org/10.1387/ijdb.123495es

Schindelin, J., Arganda-Carreras, I., Frise, E., Kaynig, V., Longair, M., Pietzsch, T., … Cardona, A. (2012). Fiji: an open-source platform for biological-image analysis. *Nature Methods*, *9*(7), 676–682. http://doi.org/10.1038/nmeth.2019

Schmidt-Nielsen, K. (1984). *Scaling: Why is Animal Size so Important?* New York: Cambridge University Press. http://doi.org/10.1016/0166-2236(85)90197-3

Schuhmann, K., Almeida, R., Baumert, M., Herzog, R., Bornstein, S. R., & Shevchenko, A. (2012). Shotgun lipidomics on a LTQ Orbitrap mass spectrometer by successive switching between acquisition polarity modes. *Journal of Mass Spectrometry*, *47*(1), 96–104.

http://doi.org/10.1002/jms.2031

Schuhmann, K., Thomas, H., Ackerman, J. M., Nagornov, K. O., Tsybin, Y. O., & Shevchenko, A. (2017). Intensity-independent noise filtering in FT MS and FT MS / MS spectra for shotgun lipidomics. *Analytical Chemistry*, (89), 7046–7052. http://doi.org/10.1021/acs.analchem.7b00794

Sears, R., & Calambokidis, J. (2002). *COSEWIC Assessment and Update Status Report on the Blue Whale Balaenoptera musculus Atlantic population / Pacific population in Canada*.

Smith, R. E. (1956). Quantitative relations between liver mitochondria metabolism and total body weight in mammals. *Annals of the New York Academy of Sciences*, *62*(17), 505–421. http://doi.org/10.1111/j.1749-6632.1956.tb35360

Spandl, J., White, D. J., Peychl, J., & Thiele, C. (2009). Live cell multicolor imaging of lipid droplets with a new dye, LD540. *Traffic*, *10*(11), 1579–1584. http://doi.org/10.1111/j.1600-0854.2009.00980.x

Staudt, T., Lang, M. C., Medda, R., Engelhardt, J., & Hell, S. W. (2007). 2 ,2'-Thiodiethanol : a new water soluble mounting medium for high resolution optical microscopy. *Microscopy Research and Technique*, *70*(1), 1–9. http://doi.org/10.1002/jemt

Tacon, A. G. J., & Metian, M. (2008). Global overview on the use of fish meal and fish oil in industrially compounded aquafeeds: Trends and future prospects. *Aquaculture*, *285*(1–4), 146–158. http://doi.org/10.1016/j.aquaculture.2008.08.015

Takeda, H., Nishimura, K., & Agata, K. (2009). Planarians maintain a constant ratio of different cell types during changes in body size by using the stem cell system. *Zoological Science*,

506 *26*(12), 805–13. http://doi.org/10.2108/zsj.26.805

507 Tejada-Romero, B., Evans, D. J., & Aboobaker, A. A. (2012). FACS analysis of the planarian
508 stem cell compartment as a tool to understand regenerative mechanisms. *Methods in*
509 *Molecular Biology*, *916*, 47–57. http://doi.org/10.1007/978-1-61779-980-8

510 Werner, S., Rink, J. C., Riedel-Kruse, I. H., & Friedrich, B. M. (2014). Shape mode analysis
511 exposes movement patterns in biology: Flagella and flatworms as case studies. *PLoS ONE*,
512 *9*(11), 1–21. http://doi.org/10.1371/journal.pone.0113083

513 West, G. B. (1999). The origin of universal scaling laws in biology. *Physica A*, *263*, 104–113.

514 West, G. B., & Brown, J. H. (2005). The origin of allometric scaling laws in biology from
515 genomes to ecosystems: towards a quantitative unifying theory of biological structure and
516 organization. *Journal of Experimental Biology*, *208*(9), 1575–1592.
517 http://doi.org/10.1242/jeb.01589

518 West, G. B., Brown, J. H., & Enquist, B. J. (1997). A general model for the origin of allometric
519 scaling laws in biology. *Science*, *276*(5309), 122–126.
520 http://doi.org/10.1126/science.276.5309.122

521 Whitfield, J. (2006). *In the Beat of a Heart: Life, Energy, and the Unity of Nature*. Washington,
522 DC: Joseph Henry Press. http://doi.org/10.17226/11634

523

524 **Acknowledgements**

525 We thank N. Alt, J. Richter, J. Ferria, A. Mishra, M. Toth and I. Smith for size quantifications,
526 K.-O. Linde and IKA Werke GmbH & Co. for microcalorimetry support, Passant Atallah (IPF

Dresden) and Michał Surma (Lipotype GmbH) for support with the animal mass measurements and H. Andreas and S. von Kannen for technical support. We thank the CMCB technology platform TU Dresden (EM and Histology) and the following MPI-CBG core facilities for their support: Cell technologies, Technology development studio, and scientific computing.

Author Contributions

Conceptualization: A.T., S.W., O.F., J.C.R., B.M.F., F.J.; methodology: A.T., O.F., S.W., Y.Q, O.K.; formal analysis: S.W., A.T., O.F., O.K.; investigation: A.T., O.F., S. W., J.P., O.K., Y.Q.; software: S.W.; resources: J.C.R., K.F., A.S., F.S.; data curation: S.W., A.T., O.F., O.K.; writing – original draft: A.T., S. W., O.F., J.C.R.; writing – review & editing: J.C.R., F.J., B.M.F., A.T., S.W., O.F., J.P., K.F., O.K., A.S.; visualization: A.T., S.W., O.F.; funding acquisition: J.C.R., F.J., B.M.F.; K.F. All authors read and approved of the manuscript.

Competing interests

The authors declare no competing financial interests.

Data and materials availability

All data on which the conclusions of this paper are based are presented in the figures, figure supplements or source data that was submitted with this manuscript.

548 **Materials and Methods**

549 Fitting of power laws

550 Power law exponents were obtained from linear fits (robust regression using a bisquare weighing
551 function, "robustfit" function in MATLAB) in the log-log plot. We only directly fitted the
552 measured data. If a data set is derived from several measurements (e.g. metabolic rate vs. wet
553 mass is derived from measurements of metabolic rate vs. dry mass and dry mass vs. wet mass),
554 the power law estimate is computed from the original fits of the individual measurements. The
555 respective standard error is obtained via error propagation.

556

557 Animal husbandry

558 The asexual (CIW4) strain of *S. mediterranea* was kept in plastic containers in 1X Montjuïc salt
559 water (1.6 mM NaCl, 1.0 mM $CaCl_2$, 1.0 mM $MgSO_4$, 0.1 mM $MgCl_2$,0.1 mM KCl, 1.2 mM
560 $NaHCO_3$) with 25 mg/L gentamycin sulfate. The animals were fed homogenized organic calf
561 liver paste and were fed at least one week prior to all experiments if not otherwise indicated.
562 Animals were kept at 20 ºC before and during experiments.

563

564 Measurement of planarian body size

565 Movies of gliding planarians were taken with a Nikon Multizoom AZ 100M (0.5x objective)
566 using dark field illumination (facilitates planarian body segmentation). The following camera
567 (DS-Fi1) settings were used: frame rate 3 Hz, exposure time 6 ms, 15 s movie length, 1280 x
568 960-pixel resolution, conversion factor 44 pixel/mm. Animals were placed one at a time inside a
569 Petri dish and typically 1 - 4 movies taken, depending on the animal's behaviour. Movies were
570 converted from AVI to MP4 format using Handbreak to reduce the file size. Movies were

571 subsequently analysed using custom-made MATLAB software (MathWorks, Natick,
572 Massachusetts, USA). Typically, those frames were analysed in which the animals were gliding
573 in a straight line (typically 10 frames). See also (Werner et al., 2014).
574
575 Microcalorimetry
576 Size-matched planarians were placed inside 4 ml glass ampoules (TA Instruments, Cat. No.:
577 24.20.0401) partially filled with 2 ml of planarian water and supplemented with 10 mM HEPES
578 for improved buffering. No HEPES was used in 22 out of 82 samples, however, no difference in
579 animal health and/or heat generation was observed (data not shown). The ampoules were sealed
580 with aluminium Caps (TA Instruments, Cat. No.: 86.33.0400) using a dedicated crimping tool
581 (TA Instruments, cat. #: 3339). The measurements were performed in a multichannel
582 microcalorimeter (TAMIII, TA Instruments), whereby 12 samples were measured
583 simultaneously including 1-2 controls without animals. The ampoules were first inserted half
584 way and kept in this position for 15 min in order to equilibrate with the temperature inside the
585 device. Then, ampoules were placed completely inside the respective channels whereby they
586 were sitting on top of a thermoelectric detector that measured the heat production in relation to
587 an oil bath, which was kept at a constant temperature of 20 °C. Before the actual measurements,
588 the system was left to equilibrate for another 45 min. The measurements lasted between 2-3
589 days. Animal behaviour was not controlled and the animals were able to freely move inside the
590 ampoule. Immediately after the metabolic rate measurements, animal dry mass was determined
591 by drying over night at 60 °C either on weighing paper or inside 0.5 ml tubes and subsequent
592 weighing on a microbalance (RADWAG MYA 5.2Y). The mass per animal was obtained by
593 dividing the collective mass by the number of animals.

594 Cell counting based on Histone H3 protein quantification

595 Generating standard curves for converting Histone H3 content into cell number: cells from 15
596 animals (length 5-8 mm) were dissociated and counted out by FACS essentially as previously
597 described (Tejada-Romero, Evans, & Aboobaker, 2012). Following enzymatic digestion of the
598 tissue, the resulting cell suspension was filtered through a CellTrics 50 µm mesh (Partec, Cat.
599 No.: 04-0042-2317) and incubated in Hoechst (33342) for 1.5 h on a rotator. Subsequently, cells
600 were pelleted once (700 rpm, 10 min) and the supernatant replaced with fresh CMFH. The
601 volume was adjusted to obtain a cell concentration suitable for FACS (typically $1\text{-}5 \cdot 10^6$
602 cells/ml). Following cell sorting, cells were kept on ice until further processing. Cells were
603 counted with a FACS ARIA III cell sorter (Beckton Dickinson) with standard filter settings and
604 sorted into 2 ml tubes. Typically, 10^5 cells were sorted per tube. Following FACS, cells were
605 frozen at - 80 ° C until further use.

606 Determination of total cell number in different-sized planarians using quantitative Western
607 blotting: plan area was measured using above-mentioned method (see also *Figure 2 – figure*
608 *supplement 1A-C*). Subsequently, individual animals were lysed in 6 M Urea, 2% SDS, 130 mM
609 DTT, 1 µg/ul BSA, 1 µg/ul BSA-AlexaFluor680 conjugate (ThermoFisher Scientific, Ca. No.:
610 A34787), protease inhibitor cocktail and ≥ 2.5 U/ml Benzonase Nuclease (SIGMA, Cat. No.:
611 E1014). Lysis was allowed to proceed for 1 - 1.5 h at room temperature, remaining tissue pieces
612 were completely lysed by tapping the tubes and vortexing. Meanwhile, the cells for the standard
613 curve (see above) were lysed by directly applying the lysis solution onto the frozen cells. Protein
614 concentrations were measured in 1:5 or 1:10 dilutions using a NanoDrop spectrophotometer
615 (Thermo Fisher Scientific) (absorbance at 280 nm). Finally, the samples were mixed with 4x
616 Laemmli buffer (4x stock: 400 mM DTT, 200 mM Tris-HCl, 8% SDS, 40% glycerol, 0.5 mg/ml

617 Bromophenol Blue) and incubated for 10 min at 60 °C before spinning down at 13000 rpm for 5
618 min. The samples were run on NuPAGE Novex 4-12% Bis-Tris protein gels (Invitrogen, Cat.
619 No.: NP0322BOX) in 1x MOPS running buffer (ThermoFisher Scientific, Cat. No.: NP0001).
620 The loaded volumes for the standard curve corresponded to 15000, 22500, 30000, 37500 and
621 45000 cells (linear signal range) and the volume of the whole-animal lysates was corresponding
622 to 50 µg of protein, ensuring that the samples were lying within the range of the standard curve.
623 4 technical replicates were carried out per experiment (analysis of 5 individual animals) by
624 running 2 chambers with 2 gels each at 140 mA for 1 h. Proteins were transferred onto Whatman
625 Protran nitrocellulose membrane (SIGMA, Cat. No.: Z613630) for 2 h in transfer buffer (20%
626 MeOH/1x MOPS). Membranes were blocked for 1 h at room temperature and continuous
627 agitation in 1x TBS-T (10 mM Tris base, 150 mM NaCl, 0.1% (w/v) Tween-20, pH 7.4) and 5%
628 (w/v) nonfat dry milk. Afterwards, membranes were incubated over night at 4 °C with anti-
629 Histone H3 antibody (Abcam, Cat. No.: ab1791) followed by at least 3 washes in TBS-T for 10
630 min. Membranes were then incubated with a fluorophore-conjugated secondary antibody (anti-
631 rabbit IRDye 680LT, LICOR, Cat. No.: 926-68023) diluted 1:20000 in blocking solution
632 followed by extensive washing in TBS-T (1x 5 min, 3x 10 min) and one final wash step in TBS
633 (10 min). Afterwards, membranes were dried at room temperature for at least 1 h and imaged on
634 an Odyssey SA Li-Cor Infrared Imaging System (LICOR). The relative fluorescent band
635 intensity was quantified using the gel-analysing tool in Fiji (Schindelin et al., 2012). The fraction
636 of cells from whole-animal lysates loaded onto the gel was calculated from the standard curve on
637 each blot separately. The total number of cells in the animals was calculated as follows: number
638 of cells loaded/volume loaded x total volume of original lysate. The obtained values were finally
639 averaged over all 4 technical replicates.

640 Image-based cell counting

641 First, plan area of individual animals was measured using above-mentioned method (see also
642 *Figure 2 – figure supplement 1A-C*). For cell dissociation, individual animals were placed inside
643 maceration solution (Romero & Baguñà, 1991) (acetic acid, glycerol, dH_2O at a ratio of 1:1:13
644 including 1 µg/ml BSA + 10 µg/ml Hoechst 33342, no methanol) and the total volume adjusted
645 according to animal size. The solution also contained typically about 1.3×10^6 fluorescent
646 beads/ml (FluoSpheres Sulfate Microspheres, 4 µm, red fluorescent 580/605 nm, ThermoFisher
647 Scientific, Cat. No.: F8858) the concentration of which was determined with a Neubauer
648 chamber for each experiment (including 10-18 animals). Dissociation was allowed to proceed at
649 room temperature for about 15 min after which cells of remaining tissue clumps were further
650 dissociated by taping and vortexing. Per animal, 2 µl drops of the cell suspension were pipetted
651 into 6-10 wells of a glass bottom 96-well plate (Greiner, Cat. No.: 655090) and the drops dried
652 over night at room temperature. Subsequently, the entire drops were imaged on an Operetta high-
653 content imaging system (PerkinElmer). The number of cells and beads were automatically
654 counted using an imaging pipeline built in CellProfiler (Carpenter et al., 2006) (*Figure 2 – figure*
655 *supplement 2*). The total number of cells was calculated from each separate well/drop by the
656 following formula: sum of cells in analysed images/sum of beads in analysed images x known
657 total number of beads in original cell suspension. For each animal, the calculated total cell
658 number was averaged across 9-10 wells.

659

660 Measurement of energy content using a bomb calorimeter

661 Size-matched planarians were placed inside a combustion crucible and lyophilized overnight in a
662 lyophiliser (Heto LyoLab 3000). Then, the samples were weighed on an analytical balance

663 (Sartorius Entris, readability: 0.1 mg) and the mass per animal was obtained by dividing the
664 collective mass by the number of animals – thus, allowing further conversion into organismal
665 cell numbers. Afterwards, the combustion enthalpy was measured by combustion in the presence
666 of high pressure O_2 inside a bomb calorimeter (IKA C 6000 global standards) running in
667 adiabatic mode. Benzoic acid pellets (IKA C723, Cat. No.: 0003243000) were used as a standard
668 for calibration as well as a burning aid for the samples. In between lyophilizing and combustion,
669 the samples were kept inside a drying chamber to prevent humidification.
670
671 Dry and wet mass measurements
672 To obtain the dry mass versus area and dry mass versus length scaling laws, the plan area of
673 individuals animals was measured using aforementioned method. Afterwards, animals were
674 individually placed on round pre-weighed glass cover slips and dried over night at approximately
675 60 °C. Subsequently, each animal was weighed 3 times on an analytical microbalance (Sartorius
676 Research 210 P) to obtain an average mass value. Wet mass was measured by removing as much
677 of residual water as possible while individual animals were placed inside a 0.5 ml tube. After
678 further exposing the animals to air for 30-40 min to evaporate remaining water outside of the
679 animal, animals were weighed on a microbalance (RADWAG MYA 5.2Y).
680
681 Food intake assay
682 Plan area of individual animals (two and three weeks starved) was measured using the above-
683 mentioned method (see also *Figure 2 – figure supplement 1A-C*). Planarians were fed with
684 organic homogenized calf liver paste, which was mixed with about $6.5*10^5$ per 1 µl liver red
685 fluorescence beads (FluoSpheres Sulfate Microspheres, 4 µm, fluorescent 580/605 nm,

686 ThermoFisher Scientific, Cat. No.: F8858) coated in 1mg/ml BSA. Single animals (or for
687 calibration 2 µl of liver/beads mix) were dissociated into single cells in maceration solution (see
688 above) containing 0.1% Tween-20 and about 300/µl yellow-green fluorescence beads
689 (FluoSpheres Sulfate Microspheres, 4 µm, fluorescent 505/515 nm, ThermoFisher Scientific,
690 Cat. No.: F8859) for volume normalization (see further below). 1 µl drops of the animal and liver
691 macerates as well as from maceration solution only were distributed into 10 wells of a glass
692 bottom 96-well plate (Greiner, Cat. No.: 655090) and dried over night at room temperature in the
693 dark. Whole drops were imaged on an Operetta high content imaging system (PerkinElmer) and
694 the number of red and yellow-green beads were automatically counted using CellProfiler
695 (Carpenter et al., 2006). The volume of liver eaten per animal was calculated as follow:

696 1. Total number of red beads per 1 animal = Number of red beads in 1 µl drop of worm
697 suspension x Total volume of original maceration solution
698 2. Total number of red beads per 1 µl liver = (Number of red beads in 1 µl drop of liver
699 suspension / 2) x Volume of maceration solution
700 3. Volume of liver eaten per animal = Total number of red beads per 1 animal / Total
701 number of red beads per 1 µl liver

702 To account for possible pipetting errors leading to variation in drop volumes, the volume of liver
703 eaten per animal was normalized to the ratio between yellow-green beads in the drops of the
704 animal macerate and in the drops of maceration solution only.

705

706 <u>Lipid droplet stain</u>

707 Two weeks starved small worms were killed in 5 % N-Acetyl-Cystein (NAC) and large worms
708 in 7.5 % NAC (5 min at room temperature) and fixed in 4 % PFA for 2 days at 4ºC. Fixed worms

709 were embedded in 4 % low-melting-point agarose and sectioned using a vibratome (100 µm,
710 Leica, Germany). Sections were treated with 0.5 % Triton X-100 in PBS for 2h and incubated in
711 PBS with lipid droplet dye LD540 (kind gift from Christoph Thiele, Bonn) (0.5 µg/ml) and
712 DAPI (1 µg/ml) overnight at room temperature. After thoroughly washing with 0.3% Triton X-
713 100 in PBS and a short rinse in PBS, the sections were optically cleared with the slightly
714 modified SeeDB protocol (Ke, Fujimoto, & Imai, 2013) as follows: Sections were incubated
715 sequentially with increasing concentrations of aqueous fructose solution (25 % for 4 h, 50 % for
716 4 h, 75 % and 100 % fructose for overnight) and finally with the saturated fructose solution
717 overnight. All steps were carried out at room temperature. The sections were mounted on glass
718 slides with the SeeDB solution and confocal images were taken on a Zeiss LSM 700 inverted
719 microscope (20x objective, Zeiss Plan-Apochromat, 0.8 numerical aperture) using 80 % 2,2'-
720 Thiodiethanol (Staudt, Lang, Medda, Engelhardt, & Hell, 2007) as immersion media.
721
722 Lipid extraction and quantification by shotgun mass spectrometry
723 Synthetic lipid standards were purchased from Avanti Polar Lipids, Inc. (Alabaster, AL, USA).
724 Stocks of internal standards were stored in glass ampoules at -20°C until used for lipid
725 extraction. Planarians of different size (40 small, length ~ 4 mm; 20 medium, ~ 8 mm; and 6
726 large, ~ 16 mm) were pooled and homogenized in ice-cold isopropanol mixed with acetonitrile
727 (1:1). Analysis of lipid extracts obtained under different homogenization conditions to prevent
728 TG degradation (*Figure 4 – figure supplement 1*) was performed on HPTLC silica gel plates
729 (Merck, Cat.No.: 105633) with the solvent system n-hexane/diethylether/acetic acid (70:30:1,
730 vol/vol/vol). Lipids were visualized by spraying plates with 3 g cupric acetate in 100 ml of
731 aqueous 10 % phosphoric acid solution and heating at 180 ºC for 10 min. Protein amount in the

732 homogenates was determined by BCA. 50 µg of total protein was extracted with MTBE/MeOH
733 as described in (Sales et al., 2016; Sales, Knittelfelder, & Shevchenko, 2017; Schuhmann et al.,
734 2012). Briefly, 700 µl of 10:3 MTBE/MeOH containing one internal standard for each lipid class
735 was added to the dried homogenates. Samples were vortexed for 1h at 4 °C. Phase separation
736 was induced by adding 140 µl of water and vortexing for 15 min at 4 °C, followed by
737 centrifugation at 13400 rpm for 15 min. The upper phase was collected, evaporated and
738 reconstituted in 600 µl of 2:1 MeOH/$CHCl_3$. 15 µl of total lipid extract was diluted with 85 µl
739 4:2:1 IPA/MeOH/$CHCl_3$ containing 7.5 mM ammonium formate for mass spectrometric
740 analysis. For the measurement of phosphatidylserines (PS), 15 µl of lipid extract were diluted
741 with 85 ul 4:1 EtOH/$CHCl_3$ containing 0.1% triethylamine.
742 Mass spectrometric analysis was performed on a Q Exactive instrument (Thermo Fischer
743 Scientific, Bremen, Germany) equipped with a robotic nanoflow ion source TriVersa NanoMate
744 (Advion BioSciences, Ithaca, NY, USA) using nanoelectrospray chips with a diameter of 4.1
745 µm. The ion source was controlled by the Chipsoft 8.3.1 software (Advion BioSciences).
746 Ionization voltage was + 0.96 kV in positive and − 0.96 kV in negative mode; backpressure was
747 set at 1.25 psi in both modes by polarity switching (Schuhmann et al., 2012). The temperature of
748 the ion transfer capillary was 200 °C; S-lens RF level was set to 50 %. Each sample was
749 analysed for 5.7 min. FTMS spectra were acquired within the range of m/z 400–1000 from 0 min
750 to 1.5 min in positive and within the range of m/z 350–1000 from 4.2 min to 5.7 min in negative
751 mode at a mass resolution of R m/z 200 = 140000, automated gain control (AGC) of 3 x 10^6 and
752 with a maximal injection time of 3000 ms. Free cholesterol was quantified by parallel reaction
753 monitoring FT MS/MS within runtime 1.51 to 4.0 min. For FT MS/MS micro scans were set to
754 1, isolation window to 0.8 Da, normalized collision energy to 12.5%, AGC to 5×10^4 and

755 maximum injection time to 3000 ms. PS was measured for 1.5 min in an additional acquisition in
756 negative FTMS mode with optimized nanoMate parameters (backpressure 1.00 psi and voltage –
757 2.00 kV). All acquired data was filtered by PeakStrainer (https://git.mpi-
758 cbg.de/labShevchenko/PeakStrainer/wikis/home) (Schuhmann et al., 2017). Lipids were
759 identified by LipidXplorer software (Herzog et al., 2012). Molecular Fragmentation Query
760 Language (MFQL) queries were compiled for PC, PC O-, LPC, LPC O-, PE, PE O-, LPE, PI,
761 LPI, PA, LPA, PS, SM, TG, DG, Cer, Chol, CE lipid classes (see Table 1 for meaning of all
762 abbreviations). The identification relied on accurately determined intact lipid masses (mass
763 accuracy better than 5 ppm). Lipids were quantified by comparing the isotopically corrected
764 abundances of their molecular ions with the abundances of internal standards of the same lipid
765 class. The amount of lipids per animal was calculated based on the known volume of
766 homogenization buffer and the known number of animals. Lipid amounts were normalized to cell
767 number using the previously established scaling relationship between cell number and area
768 (*Figure 2B*) and between length and area (*Figure 2 – figure supplement 1D*).
769
770 <u>Histological staining for glycogen on planarian cross sections</u>
771 Fixation: two weeks-starved small (~ 4mm) and large (13mm -16mm) animals were anesthetized
772 and relaxed for 5 min on ice by supplementing chilled planarian water with 0.0485% w/v
773 Linalool (Sigma, L2602). Planarians were fixed in cold alcoholic Bouins fixative (15ml Picric
774 acid (saturated alcoholic solution, TCS Biosciences, Cat. No.: HS660), 12 ml 32 % PFA, 2 ml
775 glacial Acetic acid and 15 ml Ethanol) for overnight at 4ºC and washed with 70 % Ethanol for
776 following two days.

777 Paraffin embedding and sectioning: Fixed animals were dehydrated by alcohol-xylene series (1x
778 10 min in 70 % ethanol and 2x for 30 min in 96 %, 100 % ethanol and xylene, respectively).
779 Xylene was replaced by melted paraffin at 60 ºC, which was exchanged three times, after 30 min,
780 after several hours overnight and again after 30 min, which was followed by embedding. Cross-
781 sections of 10 µm thickness were obtained using a microtome (Thermofisher Scientific, Microm
782 HM355S). The sections were dewaxed and hydrated by xylene-ethanol series (2x 10 min Xylene,
783 2x 1min 100 %, 96 % and 1x1 min 70 %, 40 %, ethanol and water). Prior to staining, one of two
784 adjacent sections was treated (for 2 h, at 37 ºC) with 0.2 N acetate buffer (pH 4.8) containing
785 amyloglucosidase (0.03 U/µl) (Sigma A1602), while the other section with buffer only. By
786 rinsing the sections with water, the digested glycogen was washed out on the section treated with
787 amyloglucosidase but not on the section without enzyme treatment.
788 For glycogen visualization, we used Best's Carmine staining method. The Carmine stock and -
789 working solutions (Carmine (C.I. 75470) Carl Roth, 6859.1) as well the differentiating solution
790 were prepared as described in Romeis - Mikroskopische Technik (Mulisch & Welsch, 2010).
791 The sections were treated for 10 min with Carmine working solutions following by
792 differentiating solution 2x for 1 min. Sections were briefly rinsed with 80 % ethanol and treated
793 2x for 1 min with 100 % Ethanol and 2x for 2 min with Xylene and mounted in Cytoseal™XYL
794 (Richard-Allan Scientific; 8312-4). Stained sections were imaged with an Olympus BX61
795 Upright Microscope with 5x and 20x objectives.
796
797 Glycogen assay
798 Two weeks-starved animals were homogenized in water (40 worms of 4 mm length in 0.5 ml, 20
799 worms of 8 mm in 1ml and 10 worms of 16 mm in 1ml) using zirconia/silica beads (1.0 mm

800 diameter, Carl Roth GmbH+Co.KG, Cat.No:11079110z) at 4ºC for 10 min. After brief
801 centrifugation, the samples were flash frozen in liquid nitrogen and sonicated (Covaris S2
802 Sonicator) for 1 min. The homogenate was used for glycogen and total carbohydrate
803 quantifications. The glycogen quantification method was adapted to planarians based on a
804 protocol for *Drosophila* larvae from the C. Thummel lab (University of Utah). Heat-treated
805 homogenate (70ºC, 10 min) was centrifuged at 13400 rpm for 2 min and the supernatant was
806 taken for the measurements. The extracted glycogen was digested to glucose by
807 amyloglucosidase treatment (Sigma, Cat. No.: A1602) (0.015 U/µl of 0.2 M acetate buffer, pH
808 4.8) for 2 h at 37 ºC. The glucose content was measured using the glucose assay kit (Sigma, Cat.
809 No.: GAGO-20). The assay was performed in black 96-well glass bottom plates (Greiner Bio-
810 One, Cat. No.: 655090) and the absorption spectra was measured using Envision Microplate
811 Reader (Perkin Elmer). Additionally, to assess background levels of free glucose, the supernatant
812 without amyloglucosidase treatment was measured. Planarians do not contain free Glucose at
813 detectable levels (data not shown). Glucose and Glycogen amounts were determined using a
814 standard curve built on a glucose and glycogen dilution series, respectively. Glycogen extraction
815 using hot 30 % KOH (*Figure 4 – figure supplement 1D*) was performed as previously published
816 (Rasouli, Shokri-Afra, & Ostovar-Ravari, 2015).
817
818 <u>Total carbohydrate measurement</u>
819 Determination of total carbohydrate was carried out on whole homogenates (same as used in
820 glycogen assay) using the phenol-sulfuric acid method. In brief, the homogenate was heated with
821 the 96% H_2SO_4 at 90ºC for 15 min, mixed with phenol (saturated with 0.1M citrate buffer, pH
822 4.3, Sigma, Cat. No.: P4682) (Homogenate: H_2SO_4: phenol at a ratio of 1:5:5) and distributed

823 into a 96-well plate (Thermo Scientific Nunc, Cat. No: 167008). The absorbance was measured
824 at 492 nm Envision Microplate Reader (Perkin Elmer). Carbohydrate amounts were determined
825 using the glycogen standard curve (see previous section). The amount of glycogen and total
826 carbohydrates per animal was calculated based on the known volume of homogenisation buffer
827 and the known number of animals. Glycogen and carbohydrate amounts were normalised to
828 organismal cell number using the previously established scaling relationship between cell
829 number and area (*Figure 2B*) and between length and area (*Figure 2 – figure supplements 1D*).
830 The non-glycogen carbohydrate amount was calculated by subtracting the determined glycogen
831 from the carbohydrate amount.
832
833 Protein measurements
834 Planarians of approximately 4, 8 and 16 mm length were chosen and protein amounts were
835 determined using the Pierce 660nm Protein Assay Reagent (ThermoFisher Scientific, Cat. No.:
836 22660) according to the manufacturer's instructions. To ensure compatibility with the used lysis
837 solution (see below), the Pierce 660nm Protein Assay Reagent was complemented with Ionic
838 Detergent Compatibility Reagent (ThermoFisher Scientific, Cat. No.: 22663). Planarian lysates
839 were prepared as follows: 44 small (length 4 mm), 10 medium (8 mm) and large (16 mm)
840 animals were placed inside 1.5 ml tubes and rinsed once with dH_2O. A lysis solution containing
841 10 M Urea, 2 % s odium dodecyl sulfate (SDS), 130 mM dithiothreitol (DTT), 2.5 µg/ml
842 Benzonase (home-made) and a protease inhibitor cocktail was added and the animals incubated
843 for 10 min followed by homogenisation using a motorized plastic pestle. Volumes of lysis buffer
844 used were 235 µl for small, 335 µl for medium and 2 ml for large animals. Subsequently, lysates
845 were cleared by centrifugation at 13000 rpm for 1 minute. The assay was performed in black 96-

846 well glass bottom plates (Greiner Bio-One, Cat. No.: 655090) and the resulting absorption
847 spectra measured using a FLUOstar Omega Microplate Reader (BMG LABTECH).
848
849 Whole mount *in situ* hybridization
850 Whole mount *in situ* hybridization (WISH) was essentially performed as previously described
851 (King & Newmark, 2013; Pearson et al., 2009).
852
853 Statistics
854 All statistical analyses were carried out using GraphPad Prism version 7.0c for Mac OSX
855 (GraphPad Software, La Jolla, California, USA).
856
857 Software
858 Excel for Mac (Microsoft, Redmond, Washington, USA) and KNIME(Berthold et al., 2007)
859 (KNIME AG, Zurich, Switzerland) were used for data handling and calculations; GraphPad
860 Prism v7.0c (GraphPad Software, La Jolla, USA) was used for statistical analyses and data
861 visualization; MATLAB (MathWorks, Natick, Massachusetts, USA) was used for planarian
862 body size measurements, theoretical analysis of models, data handling and visualisation;
863 CellProfiler (Carpenter et al., 2006) was used for image analysis; Fiji (Schindelin et al., 2012)
864 was used for Western blot quantification and image processing; Adobe Photoshop CS5 and
865 Illustrator CS5 (Adobe Systems, San Jose, California, USA) were used for image processing and
866 generating figures; the manuscript was prepared for submission using Word for Mac (Microsoft,
867 Redmond, Washington, USA).
868

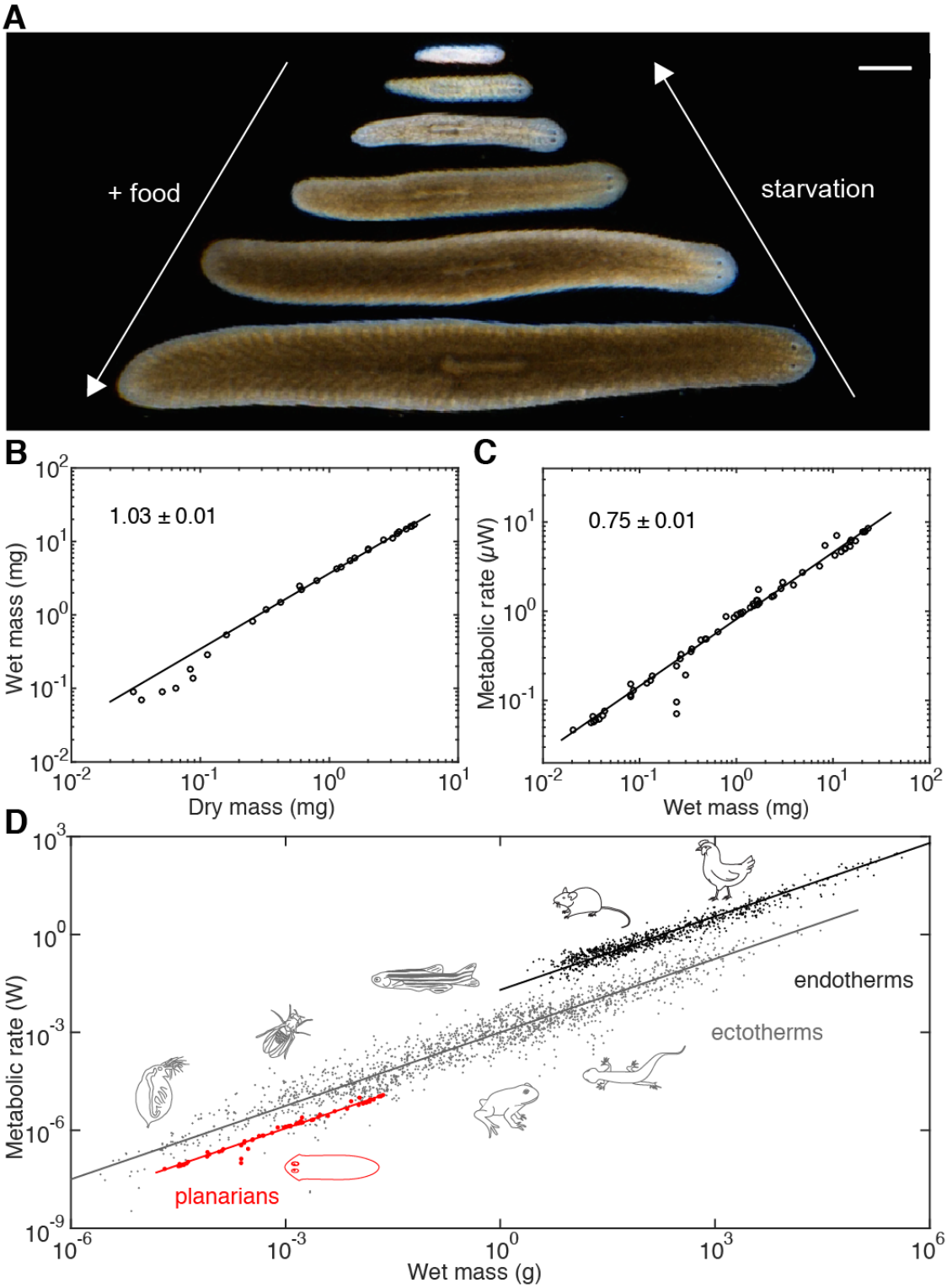

869

870 **Figure 1. Kleiber's law scaling during *S. mediterranea* body size changes.**

871 (**A**) Feeding (growth) and starvation (degrowth) dependent body size changes of *Schmidtea*
872 *mediterranea*. Scale bar, 1 mm. (**B**) Wet versus dry mass scaling with body size. The scaling
873 exponent ± standard error was derived from a linear fit for wet mass > 0.5 mg and represents the
874 exponent b of the power law $y = ax^b$. See *Figure 1 – source data 1* for numerical data. (**C**)
875 Metabolic rate versus wet mass scaling by microcalorimetry. The metabolic rate was determined
876 by a horizontal line fitted to the stabilised post-equilibration heat flow trace (*Figure 1 – figure*
877 *supplement 1*) and the post-experimental dry mass determination of all animals in the vial was
878 re-converted into wet mass by the scaling relation from (B). Each data point represents a vial
879 average of a size-matched cohort. The scaling exponent ± standard error was derived from linear
880 fits and represents the exponent b of the power law $y = ax^b$. (**D**) Metabolic rate versus wet mass
881 scaling in planarians from (C) (green) in comparison with published interspecies comparisons
882 (Makarieva et al., 2008) amongst ectotherms (grey) or endotherms (black). Dots correspond to
883 individual measurements; black and blue solid lines trace the ¾ scaling exponent; red line, linear
884 fit to the planarian data. By convention (Makarieva et al., 2008), measurements from
885 homeotherms obtained at different temperatures were converted to 37 °C, measurements from
886 poikilotherms and our planarian measurements to 25 °, using the following factor: $2^{\frac{25°C-20°C}{10\,°C}} =$
887 $2^{0.5}$ (20 °C: planarian data acquisition temperature).
888

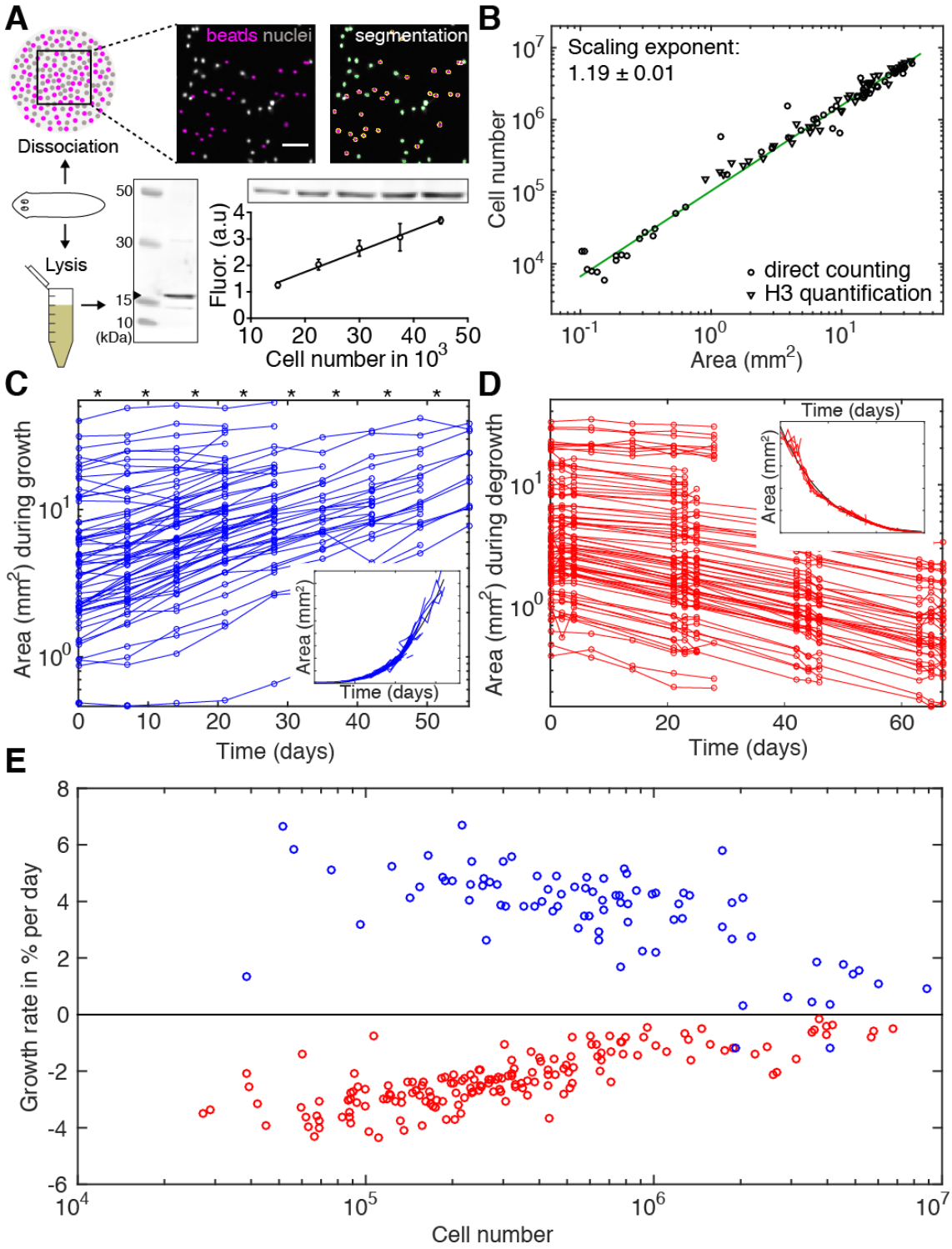

Figure 2. Growth and degrowth dynamics in *S. mediterranea*.

(**A**) Assays to measure organismal cell numbers. (Top) image-based quantification of nuclei (grey) versus tracer beads (magenta) following whole animal dissociation in presence of the

893 volume tracer beads. Bottom, Histone H3 protein quantification by quantitative Western blotting,
894 which scales linearly with the number of FACS-sorted cells (bottom right). The line represents a
895 fitted linear regression (data of 4 technical replicates) and serves as standard for calibrating the
896 H3 band in planarian lysates (bottom left) run on the same gel into cell numbers. Values are
897 shown as mean ± standard deviation. (**B**) Organismal cell number versus plan area scaling, by
898 nuclei counts (circles) or Histone H3 protein amounts (triangles) (see also *Figure 2 – supplement*
899 *1 and 2)*. The scaling exponent ± standard error was derived from a linear fit and represents the
900 exponent b of the power law $y = ax^b$. Each data point represents one individual animal and the
901 mean of several technical replicates, Histone H3 method: 9 independent experiments including 5
902 animals each; image-based approach: 4 independent experiments including 18, 10, 10 and 12
903 animals each. See *Figure 2 – source data 1-4* for numerical data. (**C**) Plan area changes of
904 individual animals during growth. * indicate feeding time points (1x per week). Inset,
905 concatenation of individual growth traces by area overlap. (**D**) Plan area change of individual
906 animals during degrowth. Inset, concatenation of individual degrowth traces by area overlap. (**E**)
907 Size-dependence of growth (blue) and degrowth rates (red) (see also *Figure 2 – figure*
908 *supplement 3*). Individual data points were calculated by exponential fits to traces in (C) and (D)
909 (growth: 2 overlapping time windows, degrowth: 3 overlapping time windows) and using the cell
910 number/area scaling law from (B) to express rates as % change in cell number/day. The positive
911 growth rates and negative degrowth rates are plotted on the same axis to facilitate comparison of
912 size dependence. See *Figure 2 – source data 4* for data of (C) and (D).
913

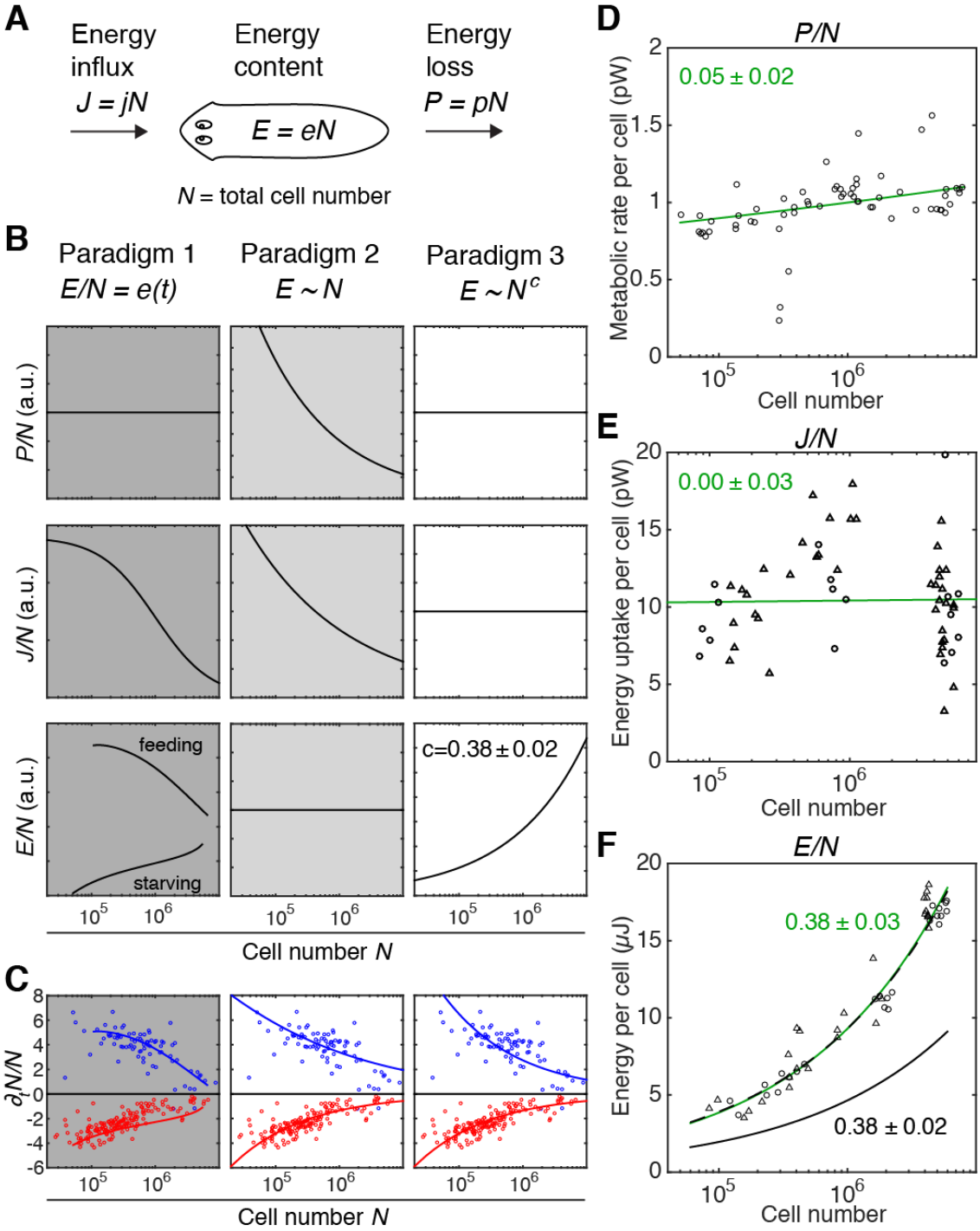

Figure 3. Size-dependent scaling of energy content explains growth/degrowth dynamics. (**A**) Planarian energy balance model. At the organismal level, changes in the physiological energy content E result from a change in the net energy influx J (feeding) and/or heat loss P (metabolic rate). Dividing E, J and P by the total cell number N approximates the energy balance

919 on a per-cell basis. (**B**) Three hypothetical control paradigms of *E* during growth and degrowth
920 (columns), which make specific predictions regarding the size-dependence of *J/N*, *E/N* and *P/N*
921 (rows). Prediction traces and scale exponents were generated by modelling the measured
922 growth/degrowth rates (*Figure 2E*) with the indicated control paradigm assumptions (see also
923 *Figure 3 – figure supplement 1-3*). (**C**) Fit of the three control paradigms to the measured
924 growth/degrowth rates (Fig. 2E). (**D**) Metabolic rate per cell (*P/N*) versus organismal cell
925 number (*N*). Data points were derived by conversion of the measurements from the metabolic
926 rate/dry mass scaling law (*Figure 1 – figure supplement 1B*) via the measured cell number/plan
927 area (*Figure 2B*) and plan area/dry mass conversion laws (*Figure 3 – figure supplement 3A*). The
928 scaling exponent ± standard error was derived from the respective linear fits (green line) and
929 represents the exponent *b* of the power law $y = ax^b$. (**E**) Energy uptake per cell versus organismal
930 cell number (*N*). Data points reflect single-animal quantifications of ingested liver volume per
931 plan area as shown in *Figure 3 – figure supplement 3D*, converted into energy intake/cell using
932 the plan area/cell number scaling law (Fig. 2B) and the assumption that 1 µl of liver paste
933 correspond to 6.15 J ("Nutrient report of calf liver," 2016; Overmoyer, McLaren, & Brittenham,
934 1987). Circles, 2 weeks-starved and triangles, 3 weeks-starved animals. The scaling exponent ±
935 standard error was derived from linear fits (green line) and represents the exponent b of the
936 power law $y = ax^b$. (**F**) Energy content per cell (*E/N*) versus organismal cell number (*N*). Data
937 points reflect bomb calorimetry quantifications of heat release upon complete combustion of size
938 matched cohorts of known dry mass as shown in *Figure 3 – figure supplement 3E*, converted via
939 the measured cell number/plan area (Figure 2B) and plan area/dry mass conversion laws (*Figure*
940 *3 – figure supplement 3A*). Circles, 1 week-starved and triangles, 3 weeks-starved animals. The
941 scaling exponent ± standard error was derived from linear fits (green line) to the data and

942 represents the exponent b of the power law $y = ax^b$. Solid black line, prediction from model 3 for
943 the physiological energy content per cell assuming a constant metabolic rate P/N = 1 pW.
944 Dashed line corresponds to respective prediction under the assumption that the physiological
945 energy (solid black line) amounts to 50 % of combustible gross energy in the animal. See *Figure*
946 *3 – source data 1* for numerical data of (C)-(F).
947

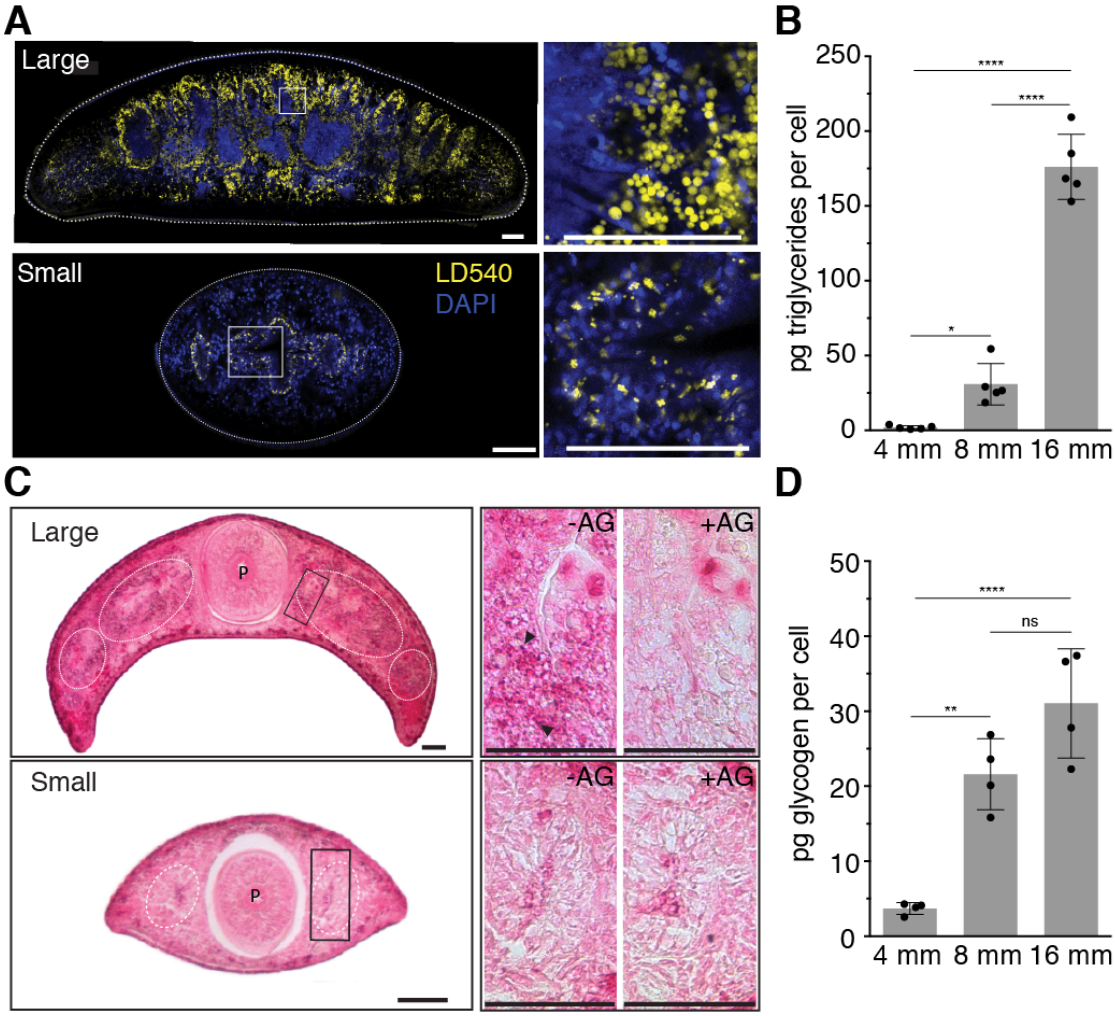

948

949 **Figure 4. Size-dependence of lipid and glycogen storage.**

950 (**A**) Lipid droplet (LD540, yellow) (Spandl et al., 2009) and nuclei (DAPI, blue) staining of pre-
951 pharyngeal transverse cross sections of a large (16 mm length, top left) and a small (4 mm,
952 bottom left). Right, magnified view of the boxed areas to the left. Scale bars, 100 µm. See *Figure*
953 *4 – source data 1* for raw images. (**B**) Mass-spectrometry-based quantification of triglycerides in
954 animals of the indicated size (*Figure 4 – figure supplement 1A-B*). All values were normalised to
955 organismal cell numbers using the previously established length versus area (*Figure 2 – figure*
956 *supplement 1D*) and *N*/*A* (*Figure 2B*) scaling laws. Bars mark mean ± standard deviation. n=5
957 biological replicates consisting of 40 pooled 4 mm, 20 8 mm and 6 16 mm long animals analysed

958 in 2 technical replicates. Significance assessed by one-way ANOVA, followed by Tukey's post-
959 hoc test (*p_{adj}≤0.05, ****p_{adj}≤0.0001). See *Figure 4 – source data 2* for numerical data and
960 statistics. (**C**) Histological glycogen staining (Best's Carmine method) of pre-pharyngeal
961 transverse cross sections of a large (16 mm, top left) and a small (4 mm, bottom left). White
962 circles: outline of intestine branches. P: Pharynx. Right, magnified view of the boxed areas to the
963 left (black rectangles). +AG, pre-treatment with amyloglucosidase, which degrades glycogen; -
964 AG, no pre-treatment of adjacent section. Arrow heads point to small, densely staining glycogen
965 granules. Scale bars, 100 µm. See *Figure 4 – source data 1* for raw images. (**D**) Quantification of
966 organismal glycogen content using an enzyme-based colorimetric assay in animals of the
967 indicated length (*Figure 4 – figure supplement C-F*). Bars mark mean ± standard deviation. n=4
968 biological replicates (independent experiments), 40 pooled 4 mm, 20 8 mm, 8 16 mm analysed in
969 3 technical replicates. Significance assessed by one-way ANOVA, followed by Tukey's post-hoc
970 test (ns not significant, **p_{adj}≤0.01, ****p_{adj}≤0.0001). See *Figure 4 – source data 2* for
971 numerical data and statistics.

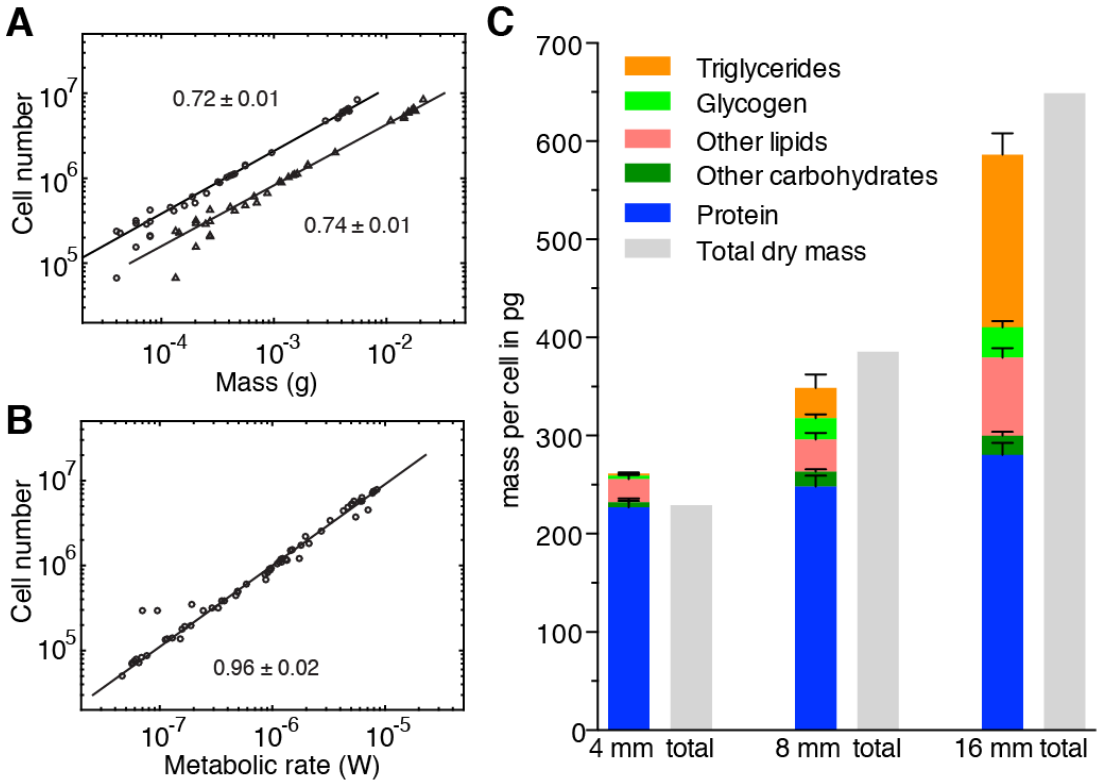

Figure 5. Size-dependent energy storage explains Kleiber's law scaling. (**A**) Cell number versus dry mass (circles) or wet mass (triangles) based the data from *Figure 3 – figure supplement 3A*. Cell numbers were converted from area using the *N*/*A* scaling law (*Figure 2B*). Dry and wet mass conversion is given by *Figure 1B*. Scaling exponents ± standard errors were derived from respective linear fits and represent the exponent b of the power law $y = ax^b$ (**B**) Cell number versus metabolic rate, derived from *Figure 1B* with scaling laws of *Figure 2B* and *Figure 3 – figure supplement 3A*. The scaling exponent ± standard error was derived from respective linear fits and represents the exponent b of the power law $y = ax^b$. (**C**) Mass composition (coloured) and total dry mass (grey) per cell in animals of the indicated body length. Triglyceride and glycogen measurements are taken from *Figure 4B* and *4D*. Quantification of other (polar and non-polar) lipids is based on the mass-spectrometry data from *Figure 4B* (n=5 biological replicates; p_{adj}=0.1720 (no significance) 8 vs. 4 mm, p_{adj}<0.0001 16 vs. 4 mm,

985 p_{adj}<0.0001 16 vs. 8 mm; 2 technical replicates). Other carbohydrates represent total
986 carbohydrate minus glycogen. n=4 biological replicates (independent experiments), 40 pooled 4
987 mm, 20 8 mm, 8 16 mm long animals; p_{adj}=0.0047 8 vs. 4 mm, p_{adj}=0.0005 16 vs. 4 mm,
988 p_{adj}=0.2790 16 vs. 8 mm; 3 technical replicates. Protein content was measured colorimetrically.
989 n=4 biological replicates (independent experiments), 44 pooled 4 mm, 10 8 mm, 10 16 mm long
990 animals; p_{adj}=0.0020 8 vs. 4 mm, p_{adj}<0.0001 16 vs. 4 mm, p_{adj}=0.0007 16 vs. 8 mm) (see also
991 *Figure 5 – figure supplement 1*). Significance was assessed by one-way ANOVA followed by
992 Tukey's post-hoc test. All values were normalised to the total cell number using the previously
993 established length-area (*Figure 1 – figure supplement 1D*) and *N*/*A* (*Figure 2B*) scaling laws.
994 Total dry mass was independently measured (*Figure 3 – figure supplement 3A*) and correlated
995 with length using the length-area relationship (*Figure 1 – figure supplement 1D*). All values are
996 shown as mean ± standard deviation. See *Figure 5 – source data 1* for numerical data and
997 statistics.
998

Figure supplements

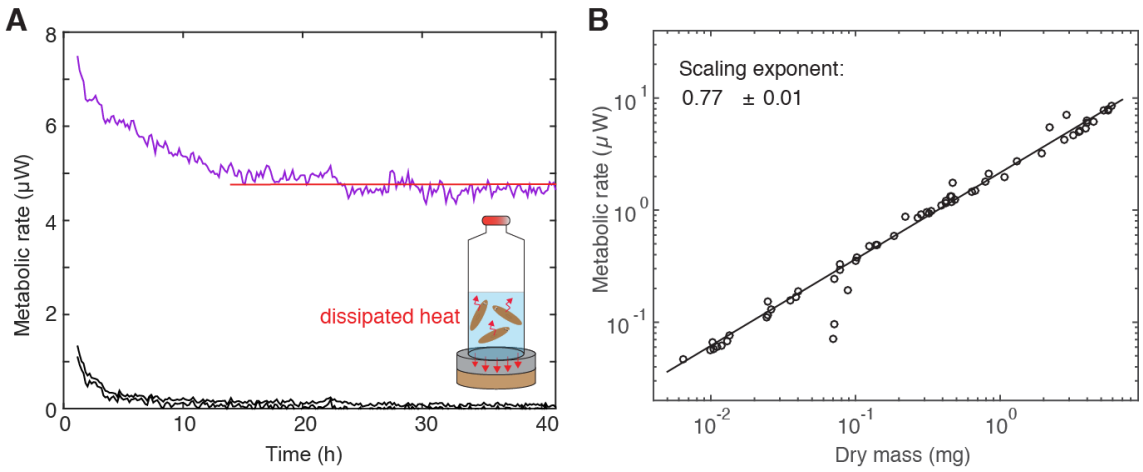

Figure 1 – figure supplement 1. Measurement of metabolic rate.

(**A**) Cartoon of a vial with enclosed animals placed on a thermo-electric detector and representative metabolic rate (heat flow) trace with an initial equilibration followed by a stable phase. The thermo-electric detector measures the heat production relative to an oil bath kept at constant temperature. The average metabolic rate was determined by manually fitting a horizontal line (red). The first 10 h were always excluded because of the initial relaxation of the control signal (medium only) which is shown in black. For individual samples, the relaxation time has been estimated to be larger than 10 h. For 21 out of 83 samples, no fit could be obtained due to high fluctuations of the signal. (**B**) Metabolic rate versus dry mass scaling used to plot *Figure 1C*. The scaling exponent ± standard error was derived from a linear fit and represents the exponent b of the power law $y = ax^b$. See *Figure 1 – figure supplement 1 – source data 1* for numerical data.

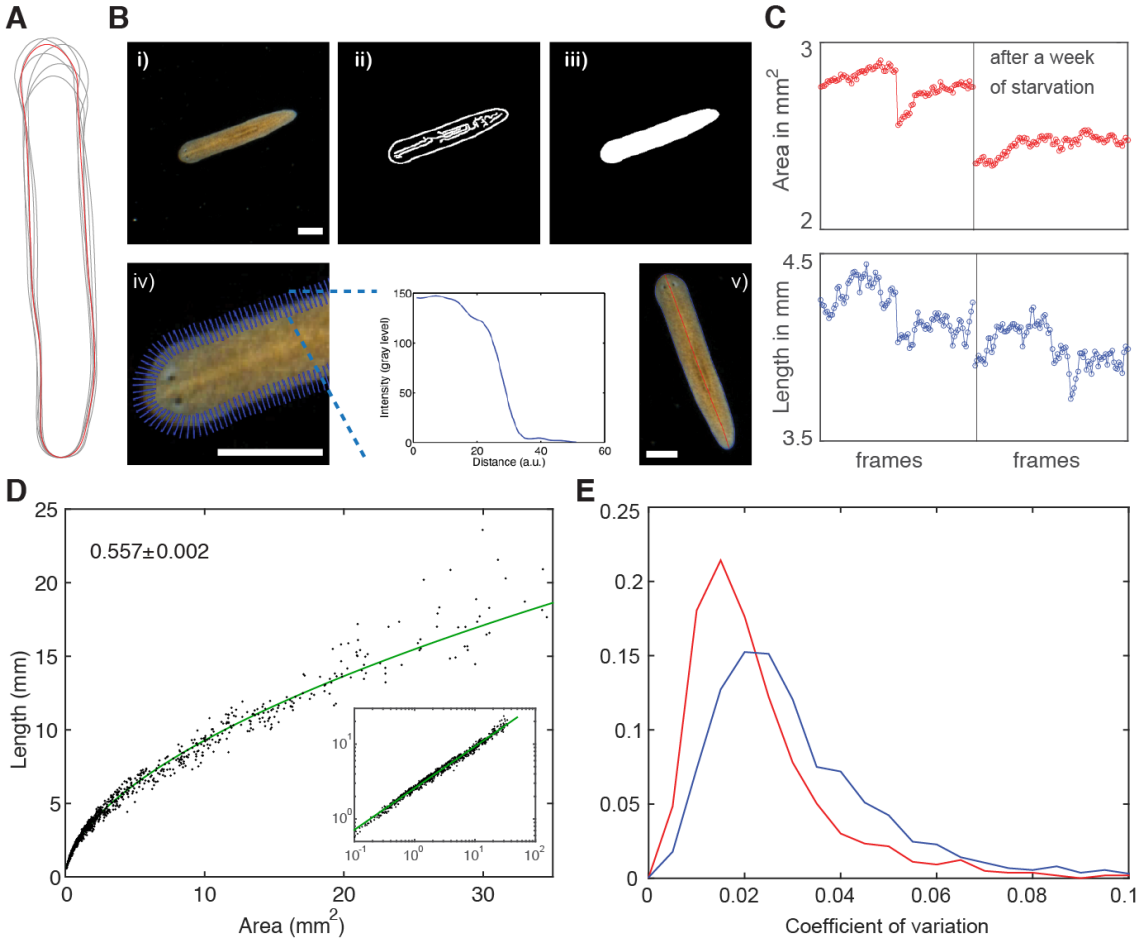

1016

1017 **Figure 2 – figure supplement 1. Measurement of planarian body size.**

1018 (**A**) Variable body outline of one individual extracted from a series of movie frames. (**B**) Pipeline
1019 for extracting plan area and length of planarians from movies, see also (Werner et al., 2014). i)
1020 raw movie frame, ii) use of Canny filter on background-corrected frames to identify edges, iii)
1021 dilation-erosion cycle to fill holes, iv) refinement of animal perimeter by finding steepest
1022 intensity across body edge, v) final boundary outline (blue) and midline (red) used to calculate
1023 area and length. Scale bars, 1 mm. See *Figure 2 – source data 4* for MATLAB script. (**C**) Area
1024 (top) and length traces (bottom) of the same individual separated by one week of starvation
1025 (compare left and right box). A drop of plan area and length reflects the expected decrease in
1026 body size and shows sensitivity, in particular of the less variable area, to small size changes. (**D**)

1027 Length versus area scaling including almost 900 measurements suggests tight regulation of body
1028 shape during growth and degrowth and confirms the accuracy of our size quantification method.
1029 The scaling exponent ± standard error was derived from a linear fit and represents the exponent b
1030 of the power law $y = ax^b$. Inset shows the same data plotted on logarithmic axes. (**E**) Histogram
1031 of the coefficients of variation (ratio standard deviation/mean) revealing less variability of the
1032 plan area compared to body length. See *Figure 2 – figure supplement 1 – source data 1* for data
1033 of (D) and (E).
1034

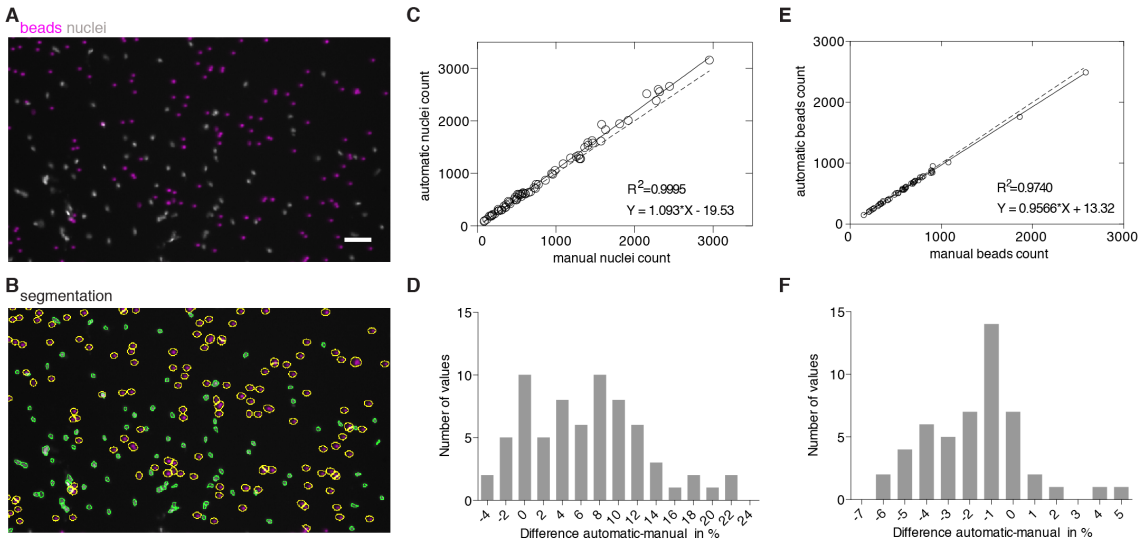

Figure 2 – figure supplement 2. Validation of image-based quantification of organismal cell number.

(**A**) Nuclei (grey) and fluorescent beads (magenta) inside a drop. (**B**) Automatic segmentation of nuclei (green contours) and beads (yellow contours). Scale bar, 25 µm. (**C**) The high correlation between automatic and manual counting methods confirms accuracy of nuclear counts (analysis of 69 images from 3 experiments). Solid line, linear regression; dotted line, hypothetical perfect match between automatic and manual counts ($y=x$). (**D**) Histogram showing the (binned) number of measured differences per image between automatic and manual counting (**E**), The high correlation between automatic and manual counting methods confirms accuracy of bead counts (analysis of 50 images from 3 experiments). Solid line, linear regression; dotted line, hypothetical perfect match between automatic and manual counts ($y=x$). (**F**) Histogram showing the number of (binned) measured differences per image between automatic and manual counting. See *Figure 2 – figure supplement 2 – source data 2* for raw images and numerical data of (C)-(F).

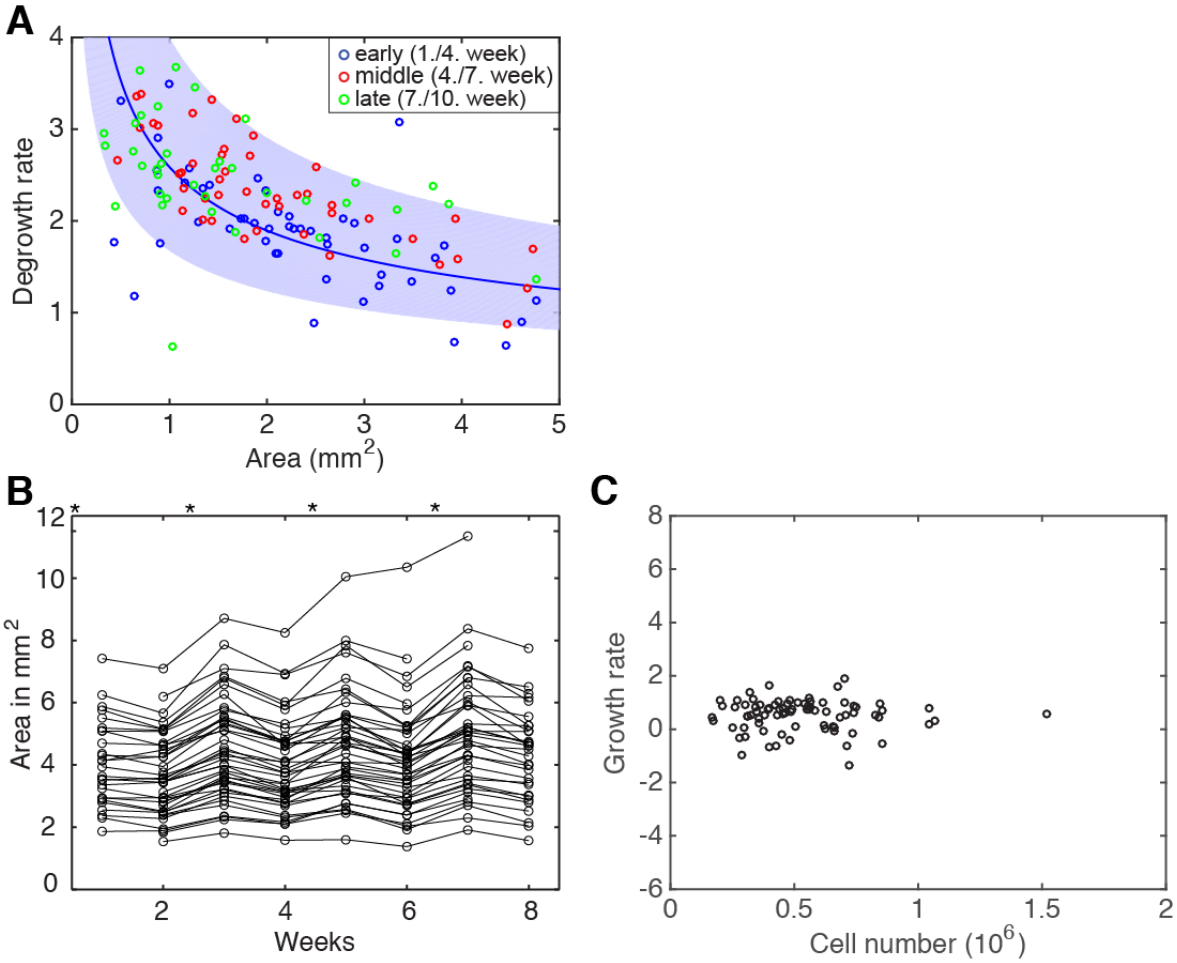

Figure 2 – figure supplement 2. Degrowth rates are independent of feeding history. (**A**) Degrowth rates from Fig. 2E colour-coded according to time since start of food deprival; early (blue), 1-4 weeks; middle (red), 4-7 weeks; late (green), 7-10 weeks. Solid line represents a power law ($y = ax^b$) fit to the early (blue) time points. Blue band represents the 95 % confidence interval for the early (blue) degrowth rates; note that middle (red) and late (green) degrowth rates lie mostly within this interval, hence, are not significantly different from the earliest points (no feeding history). (**B**) Area change of individual animals fed every second week (* indicate feeding time points). Every feeding event results in a small growth peak. While feeding every second week maintains on average a stable body size, an increased feeding frequency would cause addition of small growth peaks resulting in long-term growth. See *Figure 2 – source data*

1062 *5* for respective data. (**C**) Calculating de-/growth rates based on (B) reveals that feeding every
1063 second week, on average, results neither in growth nor in degrowth. Individual data points were
1064 calculated by exponential fits to traces in (B) across 2 time windows and using the *N*/*A* scaling
1065 law (*Figure 2B*) to express rates as % change in cell number/day.
1066

1067 **Figure 3 – figure supplement 1 (text only). Implementation of the theoretical model**

1068 The model describes the dynamic changes of total physiological energy E, defined as the fraction
1069 of energy in the body that can be metabolized and released as heat, see *Figure 3A*. The
1070 physiological energy E thus decreases due to metabolic heat production P and increases due to
1071 feeding, where J captures the net influx of physiological energy (taking into account a potentially
1072 elevated metabolism during feeding): $\dot{E} = J - P$. The dot denotes the time derivative. The
1073 average energy per cell is computed by dividing the total physiological energy by the total
1074 number of cells N: $e = E/N$. Thus, the energy per cell changes according to: $\dot{e} = j - p - Ke$,
1075 where we define $j = J/N$, $p = P/N$ and the growth rate $K = \dot{N}/N$. An increasing cell number
1076 decreases the energy per cell.

1077 Paradigm 1 assumes that cell division and cell death directly depend on the energy available per
1078 cell e. For simplicity, we consider a linear relationship between the growth rate and the energy
1079 per cell: $K = K_0(e/e_s - 1)$, with K_0 being a characteristic rate of growth and degrowth and
1080 e_s being the critical energy per cell at which planarians switch between growth and degrowth
1081 (*Figure 3 – figure supplement 2A*, dashed line). Thus, we can describe the energy dynamics by
1082 $\dot{e} = j - p - K_0(e/e_s - 1)e$. During starvation, $j = 0$ and the growth rate is decreasing, which
1083 requires $\dot{e} < 0$ (red curve). The maximum of $\dot{e}$ is at $e = e_s/2$ and from $\dot{e} < 0$ follows that $p >$
1084 $e_s K_0/4$. During feeding, where $j > p$ the curve is shifted upwards and e ends up in a growth
1085 regime (blue curve). For a constant energy influx j, the equation for $\dot{e}$ has a stable fixed point
1086 $e^* = \frac{e_s}{2} + \sqrt{(\frac{e_s}{2})^2 + \frac{(j-p)e_s}{K_0}}$ with $e^* > e_s$ for $j > 0$. Thus, the animal would grow at a constant
1087 rate $K^* = K_0(e^*/e_s - 1)$. In order for the growth rate to decrease with animal size (*Figure 2E*),

the energy influx per cell $j(N)$ must not be constant but has to be a decreasing function of N, hence, we choose $j(N) = j_0/(1 + N)$.

Figure 3 – figure supplement 2B shows a time course of the organismal cell number N when going through several rounds of feeding (blue) and starvation (red), always switching at a certain size, specifically at $N = 0.5 \cdot 10^6$ cells and $N = 4.5 \cdot 10^6$ cells (lower and upper dashed lines, respectively). In the beginning of the starvation interval, we see an overshoot where the animal still grows although feeding has stopped. As a result, we observe rather generic growth and degrowth kinetics, independent of initial values for energy and cell number or the feeding scheme, see *Figure 3 – figure supplement 2C*. Any perturbation decays quickly and there is no strong dependence on feeding history.

Paradigm 2 and 3 assume a constant relationship between cell number and physiological energy content of the worm: $E \sim N$ and $E \sim N^c$, respectively. In consequence $\dot{N}/N = \dot{E}/E$ and $\dot{N}/N = \dot{E}/(Ec)$, respectively, which can be related to metabolic rate and feeding influx via $\dot{E}/E = -P/E$ during degrowth and via $\dot{E}/E = (J - P)$/E during growth. In paradigm 2, E/N is constant, therefore both P/N and J/N have to depend on N to explain the growth and degrowth rates. In paradigm 3, both P/N and J/N can be chosen to be constant.

To fit the growth dynamics in *Figure 2C* by paradigm 1, we use the following parameters: $j_0/e_s = 14\%/d$, $p/e_s = 1.3\%/d$, $K_0 = 4.3\%/d$, initial conditions $N(0) = 3 \cdot 10^6$ and $e(0)/e_s = 1$ as well as a switch between feeding and starvation regimes at $N = 0.05 \cdot 10^6$ and $N = 6.5 \cdot 10^6$. Yet, several combinations of parameter values can fit the measurement equally well. From a fit of paradigm 2 in *Figure 2C*, we obtain $P/E = 243\, N^{-1.35}\%/d$ and $J/E = 214\, N^{-0.28}\%/d$. Finally, from a fit of paradigm 3 to the data, we obtain $E/P = 0.34\, N^{0.38} d$ and $J/P = 3.0$, see *Figure 2C*.

1111

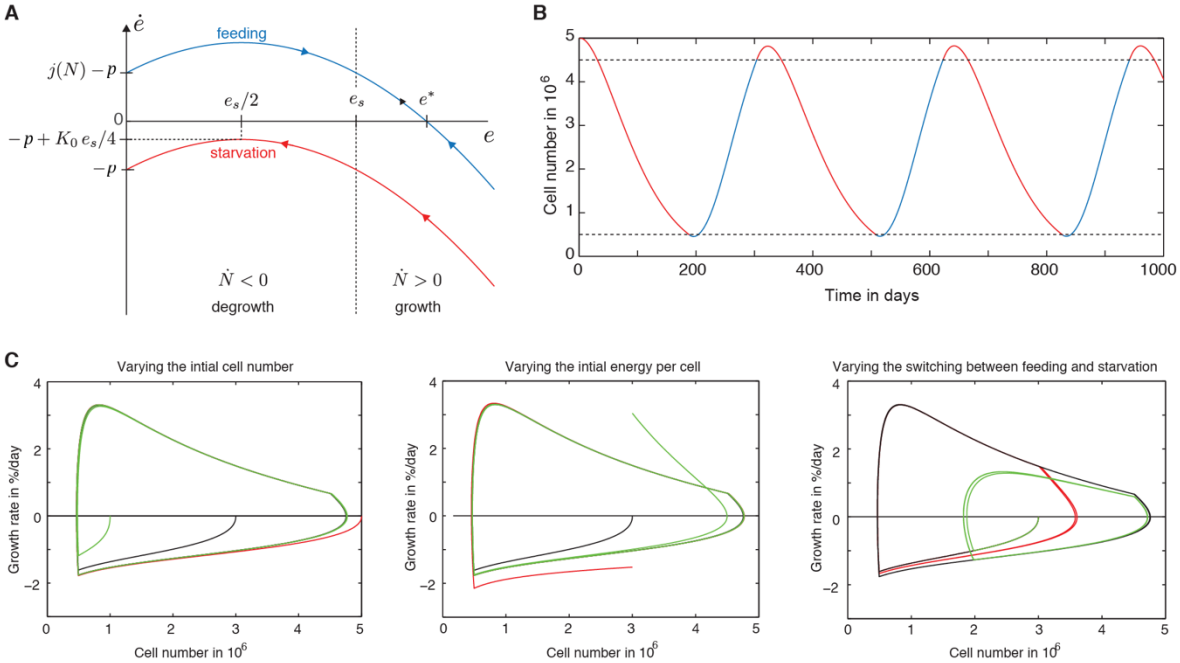

1112

1113 **Figure 3 – figure supplement 2. Further explanation of model paradigm 1.**

1114 (**A**) Dynamic behaviour of the energy content per cell during feeding and starvation in paradigm

1115 1. Graph shows the change of the energy content per cell $\dot{e}$ as a function of the energy content

1116 per cell e during starvation and feeding. See *Figure 3 – figure supplement 1* for a detailed

1117 description of paradigm 1. (**B**) Time course of the organismal cell number N when going through

1118 several rounds of feeding (blue) and starvation (red), always switching at a certain size,

1119 specifically at $N = 0.5 \cdot 10^6$ cells and $N = 4.5 \cdot 10^6$ cells (lower and upper dashed lines,

1120 respectively). In the beginning of the starvation interval, we see an overshoot where the animal

1121 still grows although feeding has stopped. (**C**) A generic growth/degrowth dynamic is observed

1122 irrespective of the initial cell number, initial energy content or the feeding scheme. Any

1123 perturbation decays quickly and there is no strong dependence on feeding history. See *Figure 3 –*

1124 *figure supplement 1* for details.

1125

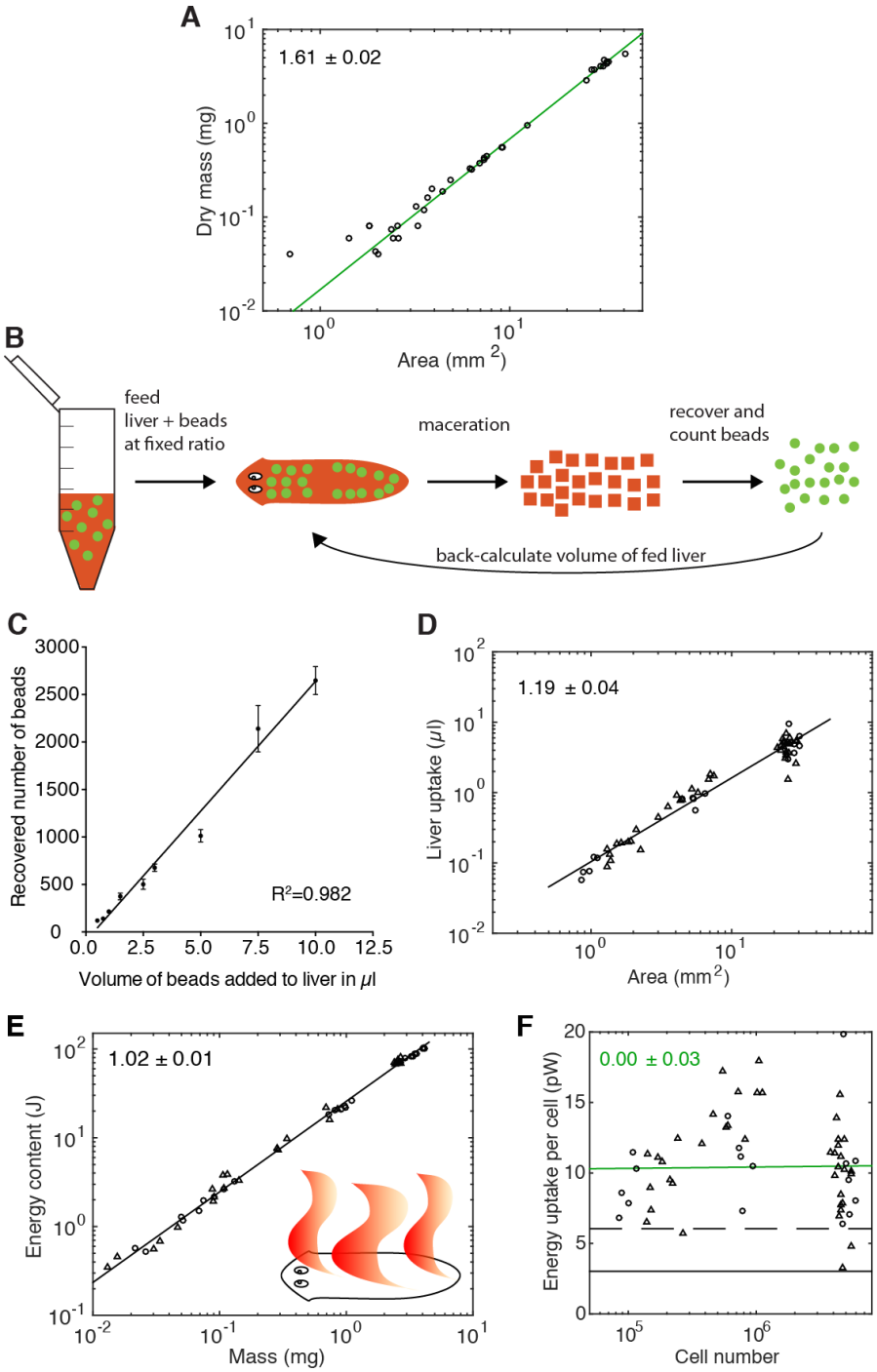

1126

1127 **Figure 3 – figure supplement 3. Paradigm validation.**

1128 (**A**) Dry mass versus plan area scaling used to convert dry mass into cell numbers (via

1129 relationship in *Figure 2B*) (each data point = one individual animal, 2 independent experiments

1130 represented with 21 and 15 animals, respectively). The scaling exponent ± standard error was

1131 derived from a linear fit and represents the exponent b of the power law $y = ax^b$. (**B**) Cartoon of
1132 food intake assay. A mixture of liver with a known concentration of spiked-in fluorescent beads
1133 as volume tracers is fed to the animals. Afterwards, individual animals are macerated and the
1134 number of recovered beads within a small volume fraction of the macerate are counted using a
1135 similar image-based approach as shown in *Figure 2A* (top). Extrapolation to the initial total
1136 sample volume reveals the total number of fed beads and finally, based on the known beads/liver
1137 ratio, the total volume of fed liver. (**C**) Recovery of a linear beads dilution series (R^2= 0.982) fed
1138 to the animals demonstrates the validity of using beads as a volume tracer. The line represents a
1139 fitted linear regression to data from one experiment; error bars, standard deviation. (**D**) Volume
1140 liver taken in as a function of plan area. Volume and area represent the original measurements
1141 based on which we calculated energy intake using the known nutritional value of calf liver
1142 ("Nutrient report of calf liver," 2016) and the density of human adult liver (Overmoyer et al.,
1143 1987) as well as organismal cell number using *Figure 2B*. Food intake is not dependent on
1144 feeding history, compare 2 weeks- (circles) with 3 weeks-starved (triangles) animals. The scaling
1145 exponent ± standard error was derived from a linear fit and represents the exponent b of the
1146 power law $y = ax^b$. (**E**) Energy content (gross calorific value) as a function of dry mass. The
1147 energy content is not dependent on feeding history, compare 1 week- (circles) with 3 weeks-
1148 starved (triangles) animals. The scaling exponent ± standard error was derived from a linear fit
1149 and represents the exponent b of the power law $y = ax^b$. See *Figure 3 – figure supplement 3 –*
1150 *source data 1* for data of (A), (D) and (E). (**F**) Food uptake per cell versus organismal cell
1151 number (N) (same data as in *Figure 3E*). Green line, fit to the data representing ingested feed
1152 energy. Scaling exponent ± standard error derived from linear fits and representing the exponent
1153 b of the power law $y = ax^b$. The black solid line represents the physiological net energy uptake

1154 (~30 % of the ingested feed energy): i.e. the net amount of energy which is assimilated by the
1155 animal body following digestion in the gut (minus energy loss due to a potential elevated
1156 metabolism during feeding) and eventually fully metabolised, thus contributing to the measured
1157 heat production (predicted from *Figure 3D*, assuming a constant metabolic rate per cell of 1
1158 pW). The conversion between gross and physiological energy (see *Figure 3F*) allows to predict
1159 the net ingested feed energy (dashed line) which is assimilated by the animal body (~60 % of
1160 ingested feed energy). This corresponds to a feed conversion ratio (ratio between feed mass and
1161 resulting gain in body mass, a measure for how efficient an organism converts feed into body
1162 mass) of ~2.6, similar to other aquatic animals (Tacon & Metian, 2008), see also
1163 discussion. Circles, 2 weeks-starved and triangles, 3 weeks-starved animals, indicate no obvious
1164 dependence on feeding history up to 3 weeks after feeding.
1165

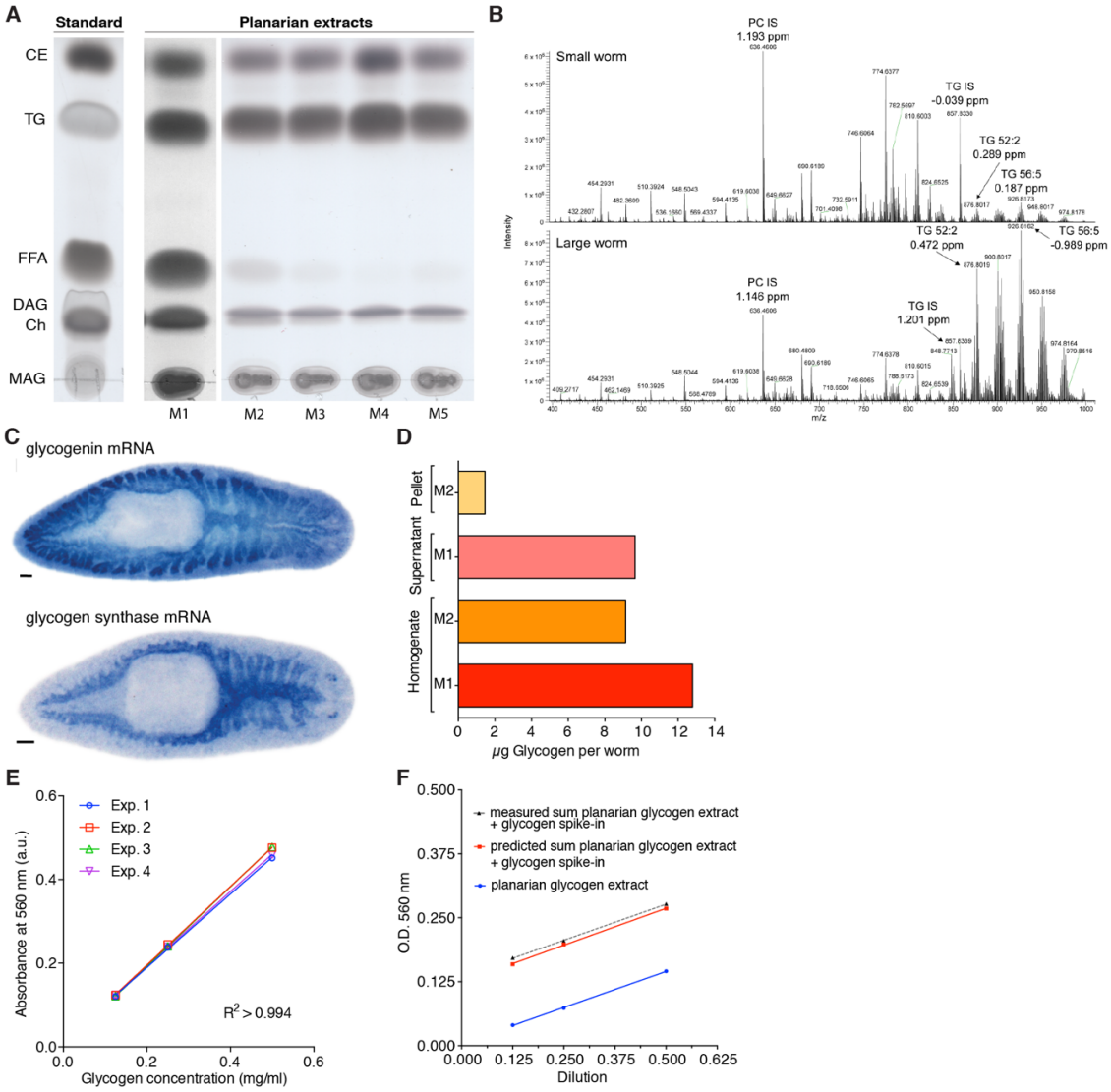

Figure 4 – figure supplement 1. Alternative assays confirm lipid and glycogen storage in planarians.

(**A**) Right, TLC (thin layer chromatography) analysis of planarian lipid extracts with different homogenization conditions to prevent triglyceride (TG) degradation: M1, Bligh and Dyer method (Bligh & Dyer, 1959); M2, 300 µl Isopropanol; M3, 1ml ice-cold Isopropanol; M4, ice-cold Isopropanol/Acetonitrile (1:1); M5, 1ml Isopropanol with 0.5% glacial acetic acid. The homogenization in ice-cold Isopropanol/Acetonitrile (1:1) generates the least amount of free fatty acids (FFAs), reflecting the least degradation rate of TGs. Left, TLC separation of the

1175 standards: CE, Cholesteryl linoleate; TG, Glyceryl trioleate; FFA, Linoleic acid; DAG,
1176 Dioleoylglycerol; Ch, Cholesterol; MAG, 1-Oleoyl-rac-glycerol. (**B**) Representative example of
1177 mass spectrum of small and large animals from positive mode (i.e. positively charged analytes).
1178 Highlighted are the internal standards for Phosphatidylcholine (PC IS) and Triglyceride (TG IS)
1179 and two of planarian endogenous Triglycerides (TG 52:2 and TG 56:5). The peak intensity of TG
1180 52:2 and TG 56:5 is almost 14-fold higher in large worms compared to small worms while the
1181 intensity of PC IS and TG IS show only minor differences (~1.3-fold small vs. large). ppm, parts
1182 per million mass accuracy. See *Figure 4 – source data 2* for quantification of relevant lipid
1183 classes. (**C**) *in situ* hybridisation against glycogenin (left) and glycogen synthase mRNA (right)
1184 further supports our finding that planarian store sugar in the form of glycogen (see also *Figure*
1185 *4C-D*). Scale bars, 100 µm. (**D**) Comparison of different glycogen extraction methods on total
1186 homogenate, supernatant and pellet fractions. M1: Water extraction, M2: hot alkali extraction.
1187 Water extraction and glycogen from the supernatant fraction were used in this study. (**E**)
1188 Glycogen standard curves from the glycogen content quantification assay. The lines represent
1189 linear regressions fitted to the data of each experiment. (n=4 independent experiments, 3
1190 technical replicates). The line represents a fitted linear regression. (**F**) Linear dilution series of
1191 planarian glycogen extract (blue line) and the predicted cumulative dilution series of extract with
1192 spiked-in glycogen (concentration =0.16 µg/ul) (red line). The predicted sums for the extract
1193 with spiked-in glycogen (red line) are closely in line with the measured sums of extract and
1194 spiked-in glycogen (dotted grey line), demonstrating the linearity of the assay across the entire
1195 concentration range. The lines represent fitted linear regressions.
1196

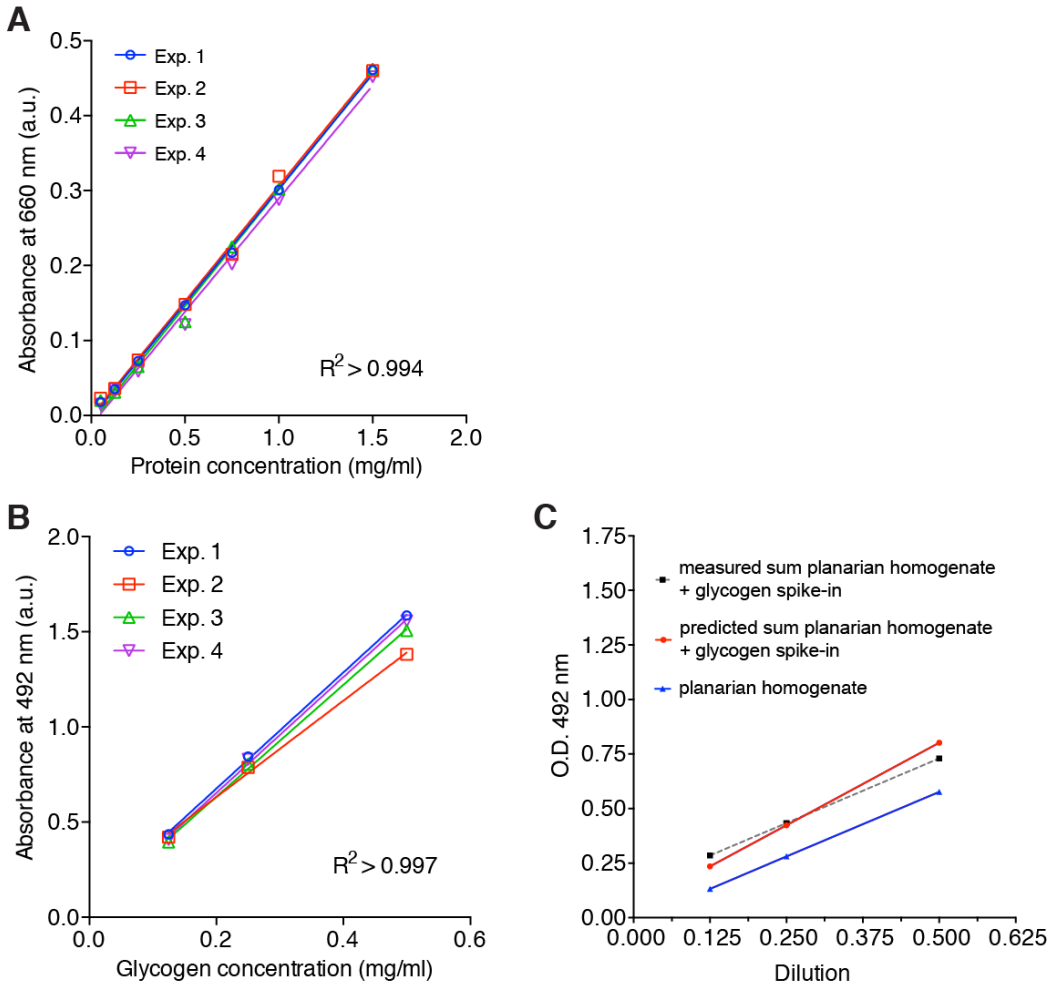

1197

1198 **Figure 5 – figure supplement 1. Standard curve protein and validation of total**
1199 **carbohydrate measurement.** (**A**) Standard curves of the colorimetric protein quantification. The
1200 lines represent linear regressions fitted to the data of each experiment (n=4 independent
1201 experiments, 3 technical replicates). (**B**) Glycogen standard curves from the phenol-sulfuric acid
1202 method. The lines represent linear regressions fitted to the data of each experiment (n=4
1203 independent experiments, 3 technical replicates). (**C**) Linear dilution series of planarian
1204 homogenate (blue line) and the predicted series of homogenate with spiked-in glycogen
1205 (conc.=0.25 µg/µl) (red line). The predicted sums for the homogenate with spiked-in glycogen
1206 (red line) are closely in line with the measured sums of homogenate and spiked-in glycogen

1207 (dotted grey line), demonstrating the linearity of the assay across the entire concentration range.

1208 The lines represent fitted linear regressions.

1209

1210

1211 **List of figure supplements**

1212

1213 Figure 1 – figure supplement 1.

1214 Measurement of body size and metabolic rate.

1215

1216 Figure 2 – figure supplement 1.

1217 Validation of image-based quantification of organismal cell number.

1218

1219 Figure 2 – figure supplement 2.

1220 Degrowth rates are independent of feeding history.

1221

1222 Figure 3 – figure supplement 1 (text only).

1223 Implementation of the theoretical model.

1224

1225 Figure 3 – figure supplement 2.

1226 Further explanation of model paradigm 1.

1227

1228 Figure 3 – figure supplement 3.

1229 Paradigm validation.

1230 Figure 4 – figure supplement 1.

1231 Alternative assays confirm lipid and glycogen storage in planarians.

1232

1233 Figure 5 – figure supplement 1.

1234 Standard curve protein and validation of total carbohydrate measurement

1235

1236

1237 **List of source data**

1238

1239 Figure – source data 1.

1240 Numerical data wet mass vs. dry mass measurements.

1241

1242 Figure 2 – source data 1.

1243 Numerical data cell number measurements.

1244

1245 Figure 2 – source data 2.

1246 Raw numerical data Histone H3 method (quantitative Western blotting)

1247

1248 Figure 2 – source data 3.

1249 CellProfiler results tables image-based approach.

1250

1251 Figure 2 – source data 4.

1252 MATLAB code for extraction of planarian body size.

1253 Figure 2 – source data 5.

1254 Numerical data growth/degrowth.

1255

1256 Figure 3 – source data 1.

1257 Numerical data for Figure 3.

1258

1259 Figure 4 – source data 1

1260 Raw images lipid droplet and glycogen.

1261

1262 Figure 4 – source data 2

1263 Raw data lipid mass spectrometry, glycogen assay and statistics tables.

1264

1265 Figure 5 – source data 1

1266 Raw data and statistics tables for measurement of other lipids, carbohydrates and protein.

1267

1268 Figure 1 – figure supplement 1 – source data 1

1269 Raw data metabolic rate measurements.

1270

1271 Figure 2 – figure supplement 1 – source data 1

1272 CellProfiler pipeline, numerical data, raw images and segmentation for validation of image-

1273 based cell counting.

1274

1275 Figure 3 – figure supplement 3 – source data 1

Numerical data for Figure 2 – figure supplement 3.

List of supplementary files

List of scaling relationships.